PHYSICAL REVIEW FLUIDS **1**, 044302 (2016)

Intrusive gravity currents propagating into two-layer stratified ambients: Vorticity modeling

M. A. Khodkar, M. M. Nasr-Azadani, and E. Meiburg
Department of Mechanical Engineering, University of California, Santa Barbara, Santa Barbara, California 93106, USA
(Received 8 March 2016; published 16 August 2016)

A simplified model is developed for intrusive gravity currents propagating along the interface of a two-layer stratified ambient. The model is based on the conservation of mass and vorticity and it does not require any empirical closure assumptions. A parametric study conducted with this model reproduces the correct behavior in various limits and is consistent with previously reported experimental observations. Specifically, it predicts the formation of equilibrium intrusions when the intrusion density equals the depth-weighted mean density of the two ambient layers. It furthermore demonstrates the existence of nonsmooth limits under certain conditions. An energy analysis shows that under nonequilibrium conditions the intrusion gains energy. The predictions by the parametric study are furthermore compared to two-dimensional direct numerical simulation results and very good agreement is observed with regard to all flow properties.

DOI: 10.1103/PhysRevFluids.1.044302

I. INTRODUCTION

Intrusions represent a special class of gravity currents that propagate horizontally into a stratified ambient at intermediate depths. They occur in a variety of atmospheric and oceanic situations, where they can influence the dynamics of flows such as sea breeze fronts, river plumes, and powder snow avalanches [1–4]. The relative ease with which intrusions can be generated in laboratory environments via lock-release processes has enabled researchers to explore them in some detail under controlled conditions and to develop simplified theoretical models for predicting features such as their thickness and front velocity [5–8]. An example of the lock-release configuration is shown in Fig. 1. Here ρ_c denotes the intermediate density of the intrusion fluid, while the densities of the lower and upper ambient layers are given by ρ_l and ρ_u, respectively. Upon removal of the gate, the intrusion develops and propagates to the right along the horizontal interface. Simultaneously, return flows evolve along the top and bottom walls in the form of left-propagating gravity currents.

The rich history of research into the dynamics of intrusions dates back at least to the investigations by Holyer and Huppert [5] and Britter and Simpson [9], who studied intrusions propagating along sharp thin interfaces. Holyer and Huppert [5] explored both bottom and interfacial currents propagating into two-layer stratified ambients. In a reference frame moving with the intrusion front, they considered the intrusion fluid to be at rest, consistent with the pioneering work of Benjamin [10], who analyzed gravity currents moving into a uniform fluid. Furthermore, they assumed that the interface ahead of the intrusion remains undisturbed. The authors enforced the conservation of mass in each of the two ambient layers, as well as the conservation of overall horizontal momentum. In addition, they assumed that energy is conserved so that Bernoulli's equation holds along each of the three interface segments. When solving the resulting system of equations for the ambient layer depths, the authors found that for a range of initial layer depths and fluid densities, the solution is nonunique, so an additional criterion is required to determine which solution will be seen in the experiment. Based on earlier studies of dissipative currents, the authors hypothesized that the energy-conserving theoretical solution that maximizes the volumetric flow rate is the one that will be observed experimentally. In this way, they obtained good agreement with corresponding experiments in terms of the intrusion front velocity. We note, however, that these experiments consider only symmetric intrusions, for which the interface ahead of the intrusion

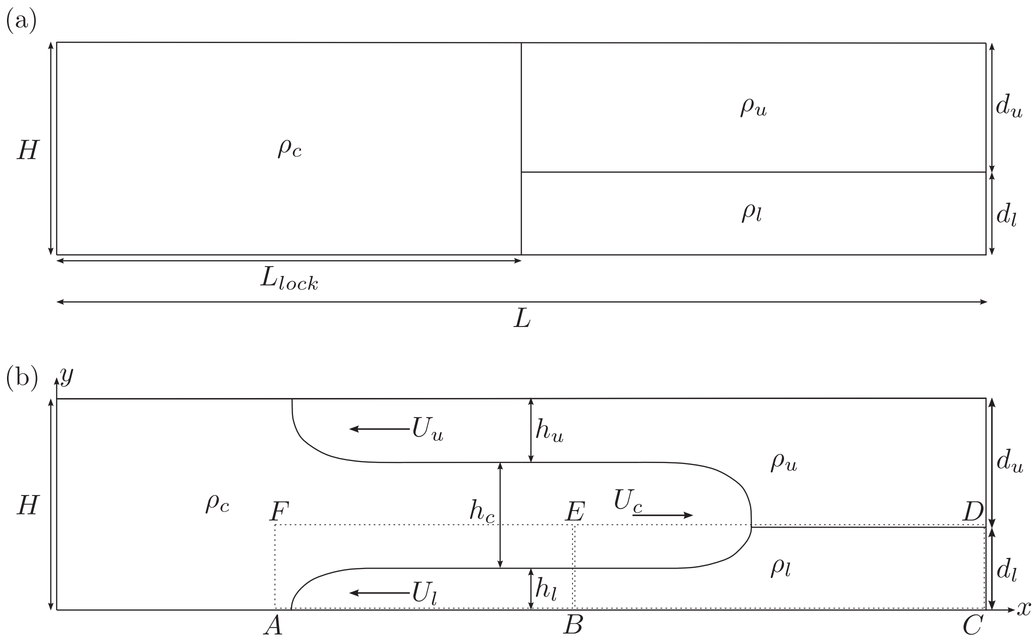

FIG. 1. Schematic of an intrusion current generated by a lock-release process: Upon removal of the gate, an intrusion of intermediate density ρ_c forms and propagates to the right along the horizontal interface separating heavy fluid of density ρ_l from light fluid of density ρ_u. Concurrently, left-propagating light and dense gravity currents emerge along the upper and lower walls, respectively. The dotted lines indicate the control volumes for which mass and vorticity conservation equations will be formulated below.

remains undisturbed. Interestingly, the theoretical arguments developed by Holyer and Huppert [5] are not limited to Boussinesq flows, but hold for arbitrary density ratios.

Britter and Simpson [9] carried out experiments for the doubly symmetric configuration, in which the ambient layers have equal depths and the intrusion density is the average of the ambient densities. They focused especially on the influence of the thickness of the interface ahead of the intrusion. de Rooij *et al.* [11] extended this line of research to particle-driven intrusions, for which they compared experimental observations with predictions by theoretical models that account for the effect of sedimentation. Further experiments on intrusive gravity currents by Lowe *et al.* [12] provided information on the detailed structure of the flow. The authors found that an approximately energy-conserving intrusion head is followed by a wake region, which is characterized by large billows that result in significant mixing and dissipation. In the tail region, by contrast, little mixing occurs and the velocity is approximately uniform. The issues of mixing and entrainment were studied further by Sutherland [13] for situations in which successive intrusions propagate into a stratified ambient so that the interfacial region gradually widens. The formation of internal and solitary waves in such configurations was investigated by Mehta *et al.* [14]. A highly resolved computational investigation into the dynamics of intrusions by Ooi *et al.* [15] reproduced many of the experimentally observed features and allowed for a detailed evaluation of the various components of the energy budget.

Sutherland *et al.* [6] simplified the theoretical approach of [5] for situations in which the density contrasts among the various fluids are small so that the Boussinesq assumption can be invoked. They defined the dimensionless parameter Δ,

$$\Delta = \frac{d_u - d_l}{H}, \tag{1}$$

which represents the relative difference in the ambient layer thicknesses (see Fig. 1) as well as ϵ,

$$\epsilon = \frac{\rho_c - \bar{\rho}}{\rho_l - \rho_u}, \tag{2}$$

which indicates the deviation of the intrusion density from the so-called equilibrium density $\bar{\rho} = \frac{\rho_l h_l + \rho_u h_u}{H}$. The case of $\epsilon = 0$ corresponds to the situation in which the intrusion density equals the depth-weighted mean density of the two ambient layers. The authors pointed out that for both the doubly symmetric case with $\Delta = \epsilon = 0$ and the simple symmetric case, also referred to as the equilibrium case, with $\Delta \neq 0$ and $\epsilon = 0$, the interface ahead of the intrusion remains flat. On the other hand, when $\epsilon \neq 0$, a leading wave forms along the interface ahead of the intrusion front. This leading wave affects the energy budget of the flow, so the discrepancy between predictions by the original, energy-conserving theory and experimental observations widens. For small nonvanishing values of ϵ, Sutherland *et al.* [6] conducted a perturbation analysis that resulted in improved agreement with experimental data.

Cheong *et al.* [7] further investigated both symmetric and nonsymmetric intrusions. They confirmed the finding by Sutherland *et al.* [6] that the interface ahead of the intrusion remains undisturbed for $\epsilon = 0$. In addition, based on the assumption that all of the initially available potential energy is converted into kinetic energy, they found that for $\epsilon = 0$ the intrusion velocity has a minimum and that for $\Delta = 0$ the speed of the intrusion does not depend on its density. The leading wave traveling ahead of the intrusion extracts relatively little energy from the flow, as will also be discussed in Sec. VI. Consequently, [7] still yields acceptable results even far from the equilibrium condition.

Flynn and Linden [8] developed a theoretical model that accounts for the influence of the upstream leading wave in nonequilibrium intrusion flows. This was accomplished by coupling the mass and streamwise momentum-conservation equations for the steady-state flow in the vicinity of the intrusion front to the two-layer shallow water equations for the propagating upstream interfacial wave. This approach, which requires an empirical assumption regarding the wave amplitude, allowed them to predict the velocity of nonequilibrium intrusions and to obtain good agreement with experimental observations.

A common theme in the above investigations is the central role of energy considerations. In addition to imposing the conservation of mass and horizontal momentum, existing theoretical models commonly assume either the validity of Bernoulli's equation along certain streamlines or the conversion of the entire initially available potential energy into kinetic energy. An alternative approach towards modeling stratified flows was recently forwarded by Borden and Meiburg [16,17], who argued that theoretical models should be based on enforcing the conservation of vertical momentum in addition to mass and horizontal momentum, rather than an energy argument. In this way, energy is free to dissipate at a rate dictated by the conservation of mass and horizontal and vertical momenta, consistent with the principles governing incompressible flow. For many models of stratified flows the conservation of vertical momentum can be enforced via the vorticity equation, which typically gives rise to algebraic relationships along individual interfaces between fluids of different densities. In this way, Borden and Meiburg [16,17] were able to develop a class of models for gravity currents and internal bores that yields better agreement with high-resolution direct numerical simulations than earlier models. As pointed out by the authors, these vorticity-based models enable us to analyze the energy budget of the flows *a posteriori*, after the flow configuration has been determined, so that the rate of energy dissipation can be evaluated explicitly, rather than be assumed *a priori*. These models were subsequently extended to non-Boussinesq flows by Konopliv *et al.* [18], to gravity currents propagating into localized or uniform shear by Nasr-Azadani and Meiburg [19], and to arbitrary ambient shear and stratification by Nasr-Azadani and Meiburg [20].

Within the present investigation, we will apply the inviscid vorticity-based modeling approach to both equilibrium and nonequilibrium intrusions in the Boussinesq limit, while the leading wave propagating ahead of the intrusion is treated as a bore. This will allow us to obtain predictions for the intrusion velocity, for the amplitude and propagation velocity of the bore, and for the thicknesses and propagation velocities of the ambient counterflows, without the need for empirical, energy-based closure assumptions. We will compare these predictions both to earlier models by other authors and to two-dimensional direct numerical simulation (DNS) Navier-Stokes results and we will analyze the energetics of the flow fields. The paper is organized as follows. In Secs. II and III we develop closed theoretical models for symmetric and nonsymmetric intrusions, based on the conservation of mass and vorticity only and without invoking any energy-related arguments. Section IV describes the setup of the corresponding DNS simulations. Section V discusses the model predictions for various flow properties, including the velocities and thicknesses of all currents and the height and speed of the leading bore. It also compares these predictions to DNS results and to earlier theoretical and experimental findings by other authors. In Sec. VI we analyze the energy budget of the flow, in order to assess the assumptions underlying earlier models. The influence of the Re and Pe values in the DNSs is discussed in Sec. VII. Section VIII summarizes the findings and presents the main conclusions.

II. SYMMETRIC INTRUSIONS

We return to Fig. 1 for a full description of the physical problem under consideration. A tank of length L and height H is divided into two compartments by means of a vertical gate. The right compartment is initially filled up to height d_l with heavy fluid of density ρ_l. A lighter fluid layer of density ρ_u and thickness d_u is placed above this dense fluid. The left compartment (the lock) of length L_{lock} contains fluid of intermediate density ρ_c so that $\rho_u < \rho_c < \rho_l$.

Upon removal of the gate, the intermediate density fluid forms a right-propagating intrusion of velocity U_c. Simultaneously, two left-propagating gravity currents emerge along the top and bottom walls: a light one of density ρ_u and height h_u and a heavy one of density ρ_l and height h_l. If these two left-propagating currents have identical front velocities $U_l = U_u$, we refer to the intrusion as symmetric or equilibrium, otherwise it is called nonequilibrium or nonsymmetric [6–8]. For symmetric intrusions, no fluid crosses the line $y = d_l$, which represents a streamline for all times. Sutherland *et al.* [6] observe experimentally that symmetric intrusions form when

$$\rho_c = \frac{\rho_l d_l + \rho_u d_u}{H}. \tag{3}$$

Flynn and Linden [8] demonstrate that this relation is equivalent to what they term the neutral buoyancy condition

$$g'_u d_u = g'_l d_l, \tag{4}$$

where $g'_l = g(\rho_l - \rho_c)/\rho_c$ and $g'_u = g(\rho_c - \rho_u)/\rho_c$. They relate this neutral buoyancy condition to the formation of two left-propagating gravity currents with identical front velocities. For the special situation of $d_l = H/2$ and $\rho_c = (\rho_l + \rho_u)/2$, the flow is geometrically symmetric with regard to $y = H/2$ and the top and bottom gravity currents have thicknesses of $H/4$ [6,9,11,14].

The symmetric intrusion case is characterized by the five unknowns U_c, U_l, U_u, h_l, and h_u. Since $y = d_l$ represents a streamline, we can solve separately for the flows below and above this line. For the lower part of the tank, the three unknowns U_c, U_l, and h_l are governed by the mass conservation equation within the control volume $BCDE$ (Fig. 1) in the reference frame moving with the front of the interfacial current

$$U_c d_l = (U_l + U_c) h_l, \tag{5}$$

as well as two vorticity conservation equations for the two fronts, while we assume that the flow is inviscid, Boussinesq, and quasisteady [16,17]. In the reference frame of the interfacial gravity current, we obtain, for the control volume $BCDE$,

$$g'_l (d_l - h_l) = \tfrac{1}{2}(U_l + U_c)^2, \tag{6}$$

and in the reference frame of the bottom current, the conservation of vorticity in control volume $ABEF$ yields

$$g_l' h_l = \tfrac{1}{2}(U_l + U_c)^2. \tag{7}$$

Solving these three equations results in

$$h_l = \frac{d_l}{2}, \tag{8}$$

$$U_c = U_l = \frac{1}{2}\sqrt{g_l' d_l}. \tag{9}$$

Corresponding considerations for the region above $y = d_l$ yield

$$h_u = \frac{d_u}{2}, \tag{10}$$

$$U_c = U_u = \frac{1}{2}\sqrt{g_u' d_u}. \tag{11}$$

This demonstrates that the condition (4) formulated by Flynn and Linden [8] for the formation of symmetric intrusions can be derived from the conservation of mass and momentum alone.

At this point, it is useful to introduce characteristic scales for length ($x_{\text{ref}} = H$), velocity ($U_{\text{ref}} = \sqrt{g'H}$), and density difference ($\rho_l - \rho_u$), where $g' = (\rho_l - \rho_u)/\rho_c$ so that we can define dimensionless variables of the form

$$x^* = \frac{x}{H}, \tag{12}$$

$$U^* = \frac{U}{\sqrt{g'H}}, \tag{13}$$

$$\rho^* = \frac{\rho - \rho_u}{\rho_l - \rho_u}. \tag{14}$$

In this way, the dimensionless solution for the case of a symmetric intrusion takes the form

$$h_l^* = \frac{d_l^*}{2}, \tag{15}$$

$$h_u^* = \frac{d_u^*}{2}, \tag{16}$$

$$U_c^* = U_l^* = U_u^* = \frac{1}{2}\sqrt{(1 - \rho_c^*) d_l^*}. \tag{17}$$

Furthermore, Eq. (3) in dimensionless form yields $\rho_c^* = d_l^*$. Hence, for symmetric intrusions the dimensionless interface height equals the dimensionless intrusion density. Consequently, we can rewrite Eq. (17) equivalently as

$$U_c^* = U_l^* = U_u^* = \tfrac{1}{2}\sqrt{\rho_c^* d_u^*} = \tfrac{1}{2}\sqrt{d_l^* d_u^*}. \tag{18}$$

Since for the symmetric case the left-propagating gravity currents and the intrusion are effectively half-depth currents in the sense of [10], it follows that they conserve energy. Hence it is not surprising that for symmetric intrusions the present results agree with those of earlier investigations in Refs. [5–8], all of which had invoked energy conservation arguments. These theoretical solutions will be compared to experimental and DNS data in Sec. V.

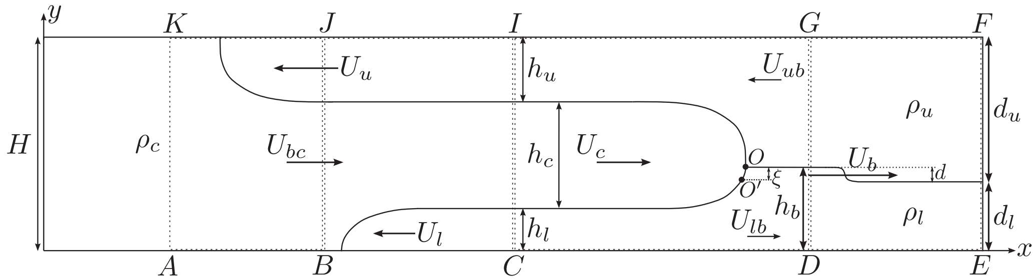

FIG. 2. Schematic of a nonsymmetric or nonequilibrium intrusion with $(\rho_c - \rho_u)/(\rho_l - \rho_u) > d_l/H$. A leading bore travels along the interface ahead of the intrusion, with a larger velocity than the intrusion itself. The dotted lines indicate the control volumes for which mass and vorticity conservation equations will be formulated below. We refer to this model as model 1 in the text.

III. NONSYMMETRIC INTRUSIONS WITH UPSTREAM LEADING BORE

When the symmetry condition (4) is not satisfied, the left-propagating gravity currents along the upper and lower walls will exhibit different front velocities. In the following, we will discuss and compare two different models for the resulting nonequilibrium intrusion. Model 1, depicted in Fig. 2, is inspired by the experiments of [6], which demonstrate the presence of a leading wave propagating ahead of the interfacial gravity current. In the following, we will model this leading wave as a bore. The alternative model 2, shown in Fig. 3, is based on simulation results from the present study to be discussed below. It differs from model 1 in that it also allows for the existence of an internal bore on the faster of the two left-propagating gravity currents, at the same streamwise location as the front of the slower gravity current. We will discuss the significance of including this left-propagating bore, later in Sec. V.

In contrast to the five unknowns that fully describe the symmetric problem, nonsymmetric intrusions give rise to several additional unknown variables. For the leading bore, these involve the wave speed U_b and the interface height h_b downstream of the wave, as well as the downstream upper and lower layer velocities U_{lb} and U_{ub}. In addition, we need to solve for the intrusion velocity U_{bc} in the region between the gravity current fronts, so model 1 is characterized by a total of ten unknown quantities. Hence, ten independent conservation equations are required for a full description. Model 2 results in two additional unknowns, viz., U'_u and h'_u, compared to model 1.

Corresponding to our earlier analysis of the symmetric case, we can formulate the equations for the nonsymmetric case by considering the conservation of mass and vorticity in various control

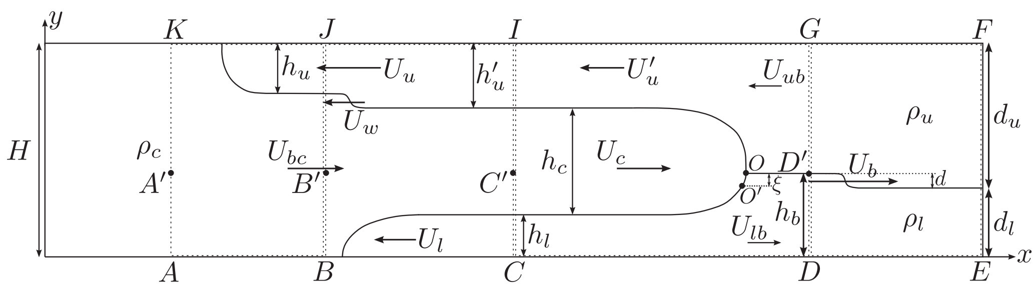

FIG. 3. Alternative model for a nonequilibrium intrusion with $(\rho_c - \rho_u)/(\rho_l - \rho_u) > d_l/H$. Here, in addition to leading bore ahead of interfacial gravity current, the faster propagating gravity current along the upper wall exhibits a bore at the same streamwise location as the front of the slower gravity current along the lower wall. The dotted lines indicate the control volumes for which mass and vorticity conservation equations will be formulated below. We refer to this model as model 2 in the text.

volumes. We begin by focusing on control volume $DEFG$, in the reference frame moving with the leading bore. It is worth mentioning, however, that we model this interfacial disturbance propagating ahead of the intrusive gravity current as a bore; some previous studies such as [8] have treated that as a nonlinear wave. Our assumption means that we suppose that this instability travels with a constant speed and the ambient interface after it will find a constant height. This is also another simplification, because some undulations will emerge along the interface, right after this instability. Regardless, these assumptions look reasonable and yield acceptable results as shown in Secs. IV and V. Mass conservation for the upper and lower layers, and vorticity conservation along the interface, give

$$U_b d_l = (U_b - U_{lb}) h_b, \tag{19}$$

$$U_b d_u = (U_b + U_{ub})(H - h_b), \tag{20}$$

$$g'(h_b - d_l) = \left(U_b + \frac{U_{ub} - U_{lb}}{2}\right)(U_{lb} + U_{ub}). \tag{21}$$

Equations (19)–(21) can be applied to both models 1 and 2, without any modifications. Next we focus on control volume $CDGI$ for model 1 shown in Fig. 2, in the reference frame moving with the intrusion. The two continuity equations for the upper and lower layers can be written in a straightforward fashion as

$$(U_c - U_{lb}) h_b = (U_c + U_l) h_l, \tag{22}$$

$$(U_c + U_{ub})(H - h_b) = (U_c + U_u) h_u. \tag{23}$$

Formulating separate vorticity conservation equations along the upper and lower interface branches requires some additional thought, as we need to determine how the vorticity inflow from the upstream of cross section GD in Figs. 2 and 3, $(U_c + \frac{U_{ub} - U_{lb}}{2})(U_{ub} + U_{lb})$, is divided between these two interface branches separating ambient fluids. In this context, a thought experiment is instructive: Imagine that in the initial configuration the upper and lower fluid layers in the right compartment are separated by an infinitesimally thin layer of fluid with density ρ_c, so there are effectively two separate interfaces connecting the left-propagating gravity current fronts to the upstream of leading bore. It is straightforward to write down the individual vorticity conservation equations for these two separate interfaces. By letting the thickness of this initial, intermediate fluid layer in the right compartment go to zero, we obtain

$$-g_l'(h_b - h_l) + \frac{g_l'}{g'}\left(U_c + \frac{U_{ub} - U_{lb}}{2}\right)(U_{ub} + U_{lb}) = -\frac{1}{2}(U_l + U_c)^2, \tag{24}$$

$$g_u'(H - h_b - h_u) + \frac{g_u'}{g'}\left(U_c + \frac{U_{ub} - U_{lb}}{2}\right)(U_{ub} + U_{lb}) = \frac{1}{2}(U_u + U_c)^2. \tag{25}$$

The corresponding equations for model 2 take the form

$$(U_c - U_{lb}) h_b = (U_c + U_l) h_l, \tag{26}$$

$$(U_c + U_{ub})(H - h_b) = (U_c + U_u') h_u', \tag{27}$$

$$-g_l'(h_b - h_l) + \frac{g_l'}{g'}\left(U_c + \frac{U_{ub} - U_{lb}}{2}\right)(U_{ub} + U_{lb}) = -\frac{1}{2}(U_l + U_c)^2, \tag{28}$$

$$g_u'(H - h_b - h_u') + \frac{g_u'}{g'}\left(U_c + \frac{U_{ub} - U_{lb}}{2}\right)(U_{ub} + U_{lb}) = \frac{1}{2}(U_u' + U_c)^2. \tag{29}$$

The control volume $BCIJ$, in the reference frame moving with the lower gravity current front, provides the vorticity equation

$$g'_l h_l = \tfrac{1}{2}(U_l + U_c)^2. \tag{30}$$

For model 2, it gives rise to additional equations for the conservation of mass and vorticity for the internal bore of the faster current

$$(U_{bc} + U_l)(H - h_u) = (U_c + U_l)(H - h_l - h'_u), \tag{31}$$

$$g'_u(h'_u - h_u) + \left(U_l + \frac{U_{bc} - U_u}{2}\right)(U_u \ \ + U_{bc}) = \left(U_l + \frac{U_c - U'_u}{2}\right)(U'_u + U_c). \tag{32}$$

The simulation results to be discussed below indicate that the internal bore of the faster gravity current is located at the same streamwise location as the front of the slower current, so

$$U_l = U_w. \tag{33}$$

The final two equations are obtained for the control volume $ABJK$, by formulating the conservation of mass and vorticity in the reference frame of the upper gravity current front

$$U_u H = (U_{bc} + U_u)(H - h_u), \tag{34}$$

$$g'_u h_u = \tfrac{1}{2}(U_u + U_{bc})^2. \tag{35}$$

Model 1 is completely described by Eqs. (19)–(25), in addition to (30), (34), and (35). Model 2, on the other hand, is governed by Eqs. (19)–(21), along with (26)–(35). Note that these respective systems of algebraic equations are closed, so they do not require any closure assumptions. Specifically, they were derived without any considerations of energy arguments. While analytical solutions for these systems of nonlinear algebraic equations cannot be obtained under general conditions, they can be solved numerically in a straightforward fashion via using a bisection root solver. The solutions, rendered dimensionless according to (12)–(14), will be discussed in the following. We remark that the numerical solution procedure gave no indication of multiple solutions anywhere in the parameter regime for models 1 and 2. This is in contrast to the models employed in the earlier investigations in Refs. [5,6], which had obtained nonunique solutions for a range of interface heights and intrusion densities.

IV. DIRECT NUMERICAL SIMULATIONS

In order to assess the validity and predictive capability of the above models, we will present comparisons with earlier models [5,7,8], as well as with direct numerical simulations of the unsteady two-dimensional Navier-Stokes equations in the Boussinesq limit. These simulations were conducted with our code TURBINS, which has been described and validated in detail in Refs. [21,22]. TURBINS is a finite-difference solver based on a fractional step projection method, along with TVD-RK3 time integration. It solves the dimensionless conservation equations for mass, momentum, and density

$$\nabla \cdot \mathbf{u}^* = 0, \tag{36}$$

$$\frac{\partial \mathbf{u}^*}{\partial t^*} + \mathbf{u}^* \cdot \nabla \mathbf{u}^* = -\nabla p^* + \frac{1}{\mathrm{Re}} \nabla^2 \mathbf{u}^* + \rho^* \mathbf{e}^g, \tag{37}$$

$$\frac{\partial \rho^*}{\partial t^*} + \mathbf{u}^* \cdot \nabla \rho^* = \frac{1}{\mathrm{Pe}} \nabla^2 \rho^*, \tag{38}$$

where $\mathbf{e}^g$ represents the unit vector in the direction of gravity and t^* is defined as t/t_{ref}, where $t_{\mathrm{ref}} = H/\sqrt{g'H}$. The dimensionless parameters in the form of a Reynolds number Re and a Péclet

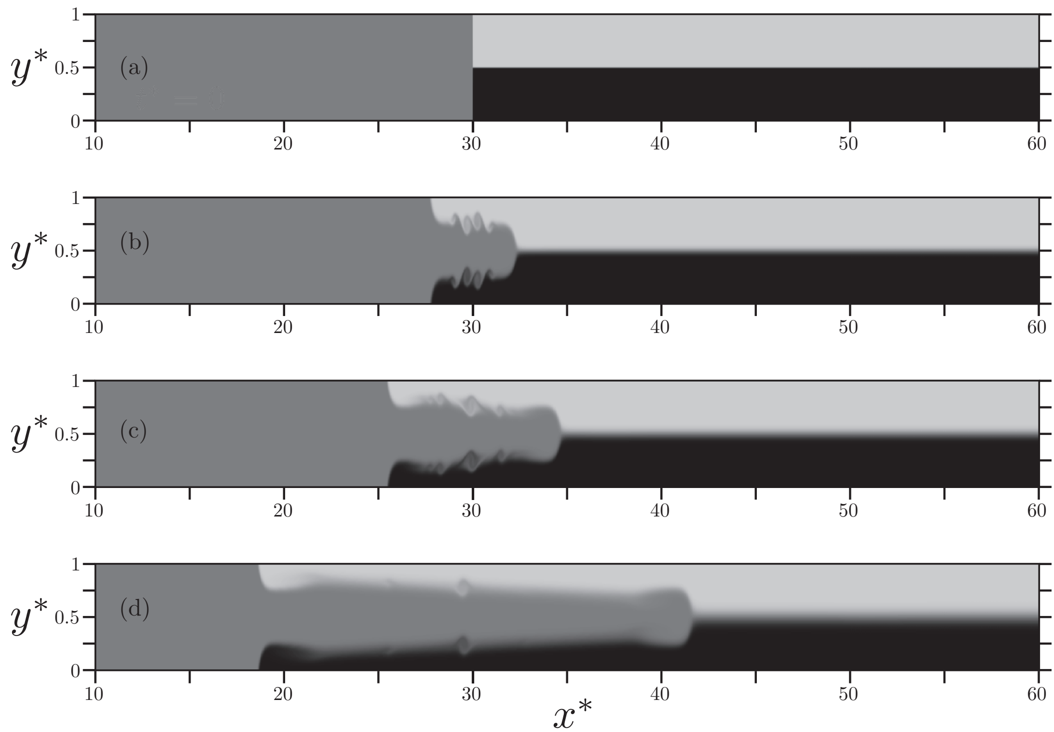

FIG. 4. Evolution of the density field for a doubly symmetric intrusion starting from rest: (a) $t^* = 0$, (b) $t^* = 10$, (c) $t^* = 20$, and (d) $t^* = 50$. In dimensionless form, the initial conditions of the problem are $\rho_c^* = d_l^* = 0.5$. The density field varies from $\rho^* = 0$ (light gray) to $\rho^* = 1$ (black).

number Pe are defined as

$$\mathrm{Re} = \frac{u_b H}{\nu}, \tag{39}$$

$$\mathrm{Pe} = \frac{u_b H}{D}. \tag{40}$$

As stated earlier, the buoyancy velocity u_b is given by $\sqrt{g'H}$, with the channel height H representing the characteristic length scale. Here ν and D indicate the kinematic viscosity and the diffusivity of the density field, respectively. We apply free slip conditions for the velocity, along with vanishing normal flux conditions for the density field, along all solid boundaries. The Reynolds and Péclet numbers are set, respectively, to 12 000 and 30 000 in the simulations, unless stated otherwise. These fairly high Re and Pe numbers result in a relatively minor influence of viscosity and diffusion on the current velocities and heights. The fluid is at rest initially, with the density field specified according to Fig. 1 as

$$\rho^* = \begin{cases} \rho_c^* & \text{for } x^* \leqslant L_{\text{lock}} \\ 1 & \text{for } x^* > L_{\text{lock}},\ y^* \leqslant d_l^* \\ 0 & \text{otherwise.} \end{cases} \tag{41}$$

The computational domain has a dimensionless length of 60 and a height of 1, and the lock length is set to 30. The computational grid has a uniform spacing of $\Delta x^* = 0.01$ and $\Delta y^* = 0.005$, which is sufficiently fine not to influence the simulation results.

Figure 4 shows the evolution of the doubly symmetric case with $d_l = H/2$ and $\rho_c = (\rho_l + \rho_u)/2$. The left-propagating gravity currents along the upper and lower walls and the right-propagating

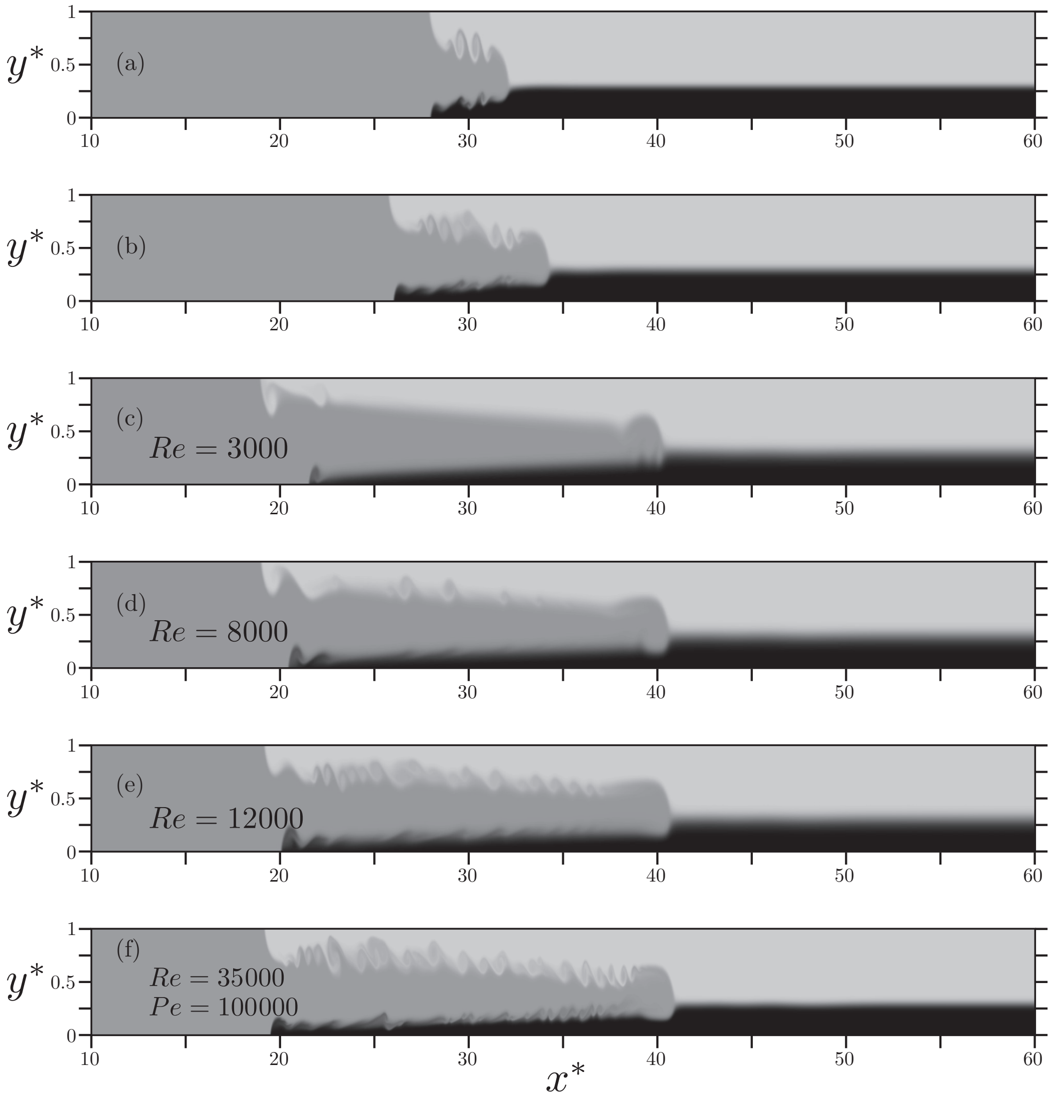

FIG. 5. Evolution of an equilibrium intrusion for $\rho_c^* = d_l^* = 0.3$: (a) $t^* = 10$, (b) $t^* = 20$, (c) $t^* = 50$ and Re = 3000, (d) $t^* = 50$ and Re = 8000, (e) $t^* = 50$ and Re = 12 000, and (f) $t^* = 50$, Re = 35 000, and Pe = 100 000. While the inviscid model predicts that the left-propagating gravity currents should have identical front velocities, the viscous simulation yields slightly different front speeds. For increasing Reynolds numbers, however, these front velocities are increasingly close to each other. As predicted by the model, the interface ahead of the intrusion remains undisturbed.

intrusion all have identical front velocities. For comparison, Fig. 5 presents the case of an equilibrium intrusion with $\rho_c^* = d_l^* = 0.3$. The slightly different front velocities of the two left-propagating gravity currents are a consequence of the finite Reynolds number in the simulation, which implies that the top and bottom currents effectively have different Reynolds numbers based on their individual heights. This is confirmed by the simulation results for Re = 3000, 8000, and 12 000 shown in Figs. 5(c)–5(e), respectively, which indicate that the front velocities of the left-propagating currents approach each other as the Reynolds number is increased. Figure 5(f) demonstrates an extreme case with Re = 35 000 and Pe = 100 000, for which the difference in the front velocities of the

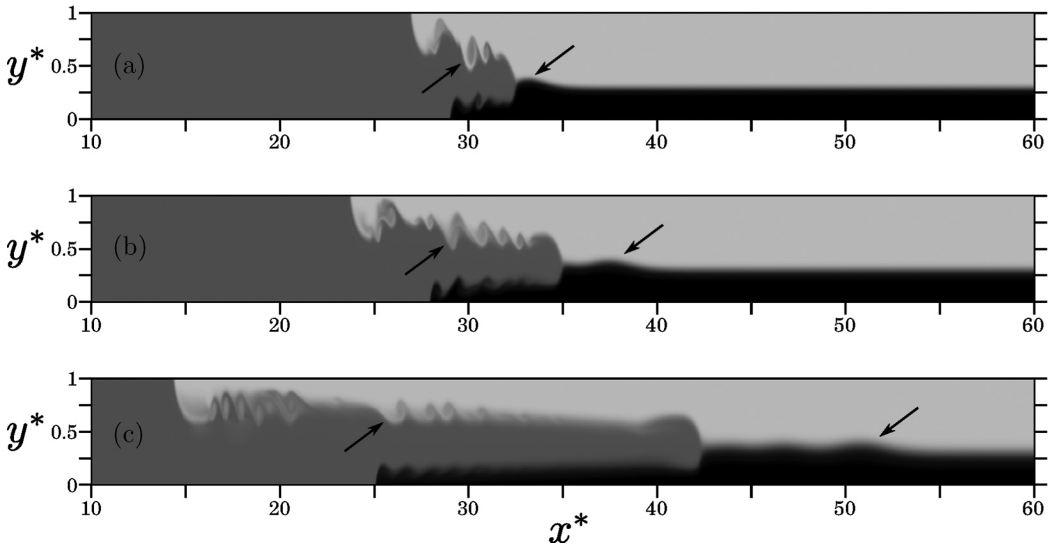

FIG. 6. Evolution of a nonsymmetric intrusion for $\rho_c^* = 0.5$ and $d_l^* = 0.3$: (a) $t^* = 10$, (b) $t^* = 20$, and (c) $t^* = 50$. For this nonequilibrium case, the left-propagating currents have different front velocities and two internal waves form: one propagates to the right ahead of the interfacial gravity current and the other one travels along the interface of the faster left-propagating gravity current, at the same streamwise location as the front of the slower current. The locations of these internal waves are indicated by arrows in the figure.

left-propagating currents has become quite small. This simulation was carried out with a resolution two times finer in the horizontal direction and three times finer in the vertical direction. In spite of the symmetry breaking due to these slightly different front velocities, we recognize that the right-propagating intrusion does not give rise to a leading bore along the horizontal interface.

Figure 6 illustrates the case of a nonequilibrium intrusion for $\rho_c^* = 0.5$ and $d_l^* = 0.3$. In this case, the front velocities of the left-propagating gravity currents along the top and bottom walls differ substantially. Along the horizontal interface separating the dense from the light fluid, the advancing intrusion causes the formation of an undular bore that propagates significantly faster than the intrusion itself. In addition, closer inspection of the upper gravity current at time $t^* = 50$ reveals the existence of a bore near the streamwise location of the lower current front, consistent with the sketch of model 2 in Fig. 3 above. Additional simulations for a broad range of ρ_c^* and d_l^* (not shown) confirm this observation. These DNS results are fully consistent with the earlier experimental observations of [6,7,9,11,14].

In order to obtain accurate values for the front velocities of all currents, we mark the fluid corresponding to each current by means of a passive scalar (dye), which is tracked in the simulation as a separate concentration field, with the same Pe value as the density field. We can then define the front position x_f^* as the location where the local dimensionless current height computed as

$$\eta^*(x^*,t^*) = \int_0^1 c_d^*(x^*,y^*,t^*)dy^* \tag{42}$$

first exceeds a value of 0.01. Here c_d^* denotes the dimensionless dye concentration and η^* indicates the local height of a current. Figure 7 provides examples for tracking the intrusion and lower gravity current fluids, respectively.

Figure 8 shows the front locations as functions of time, for the symmetric and nonsymmetric intrusions of Figs. 4–6. After an initial transient, each current propagates with a quasisteady velocity, in spite of continuously evolving interfacial instabilities and mixing. The straight line segments indicate the respective quasisteady front velocities, obtained by linear fits of the DNS results.

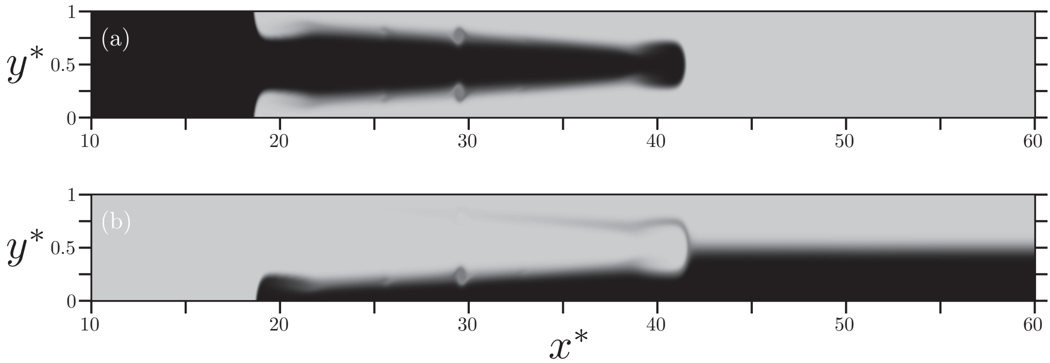

FIG. 7. By marking the fluid of each current with dye, we can evaluate the current heights and velocities, as described in detail in the text.

The quasisteady heights of the left-propagating currents are obtained as follows. For the slower one, we determine the effective height h^* by evaluating

$$h^* = \frac{\int_{x_f^*}^{L_{\rm lock}^*} \eta^*(x^*,t_s^*)dx^*}{L_{\rm lock}^* - x_f^*}, \tag{43}$$

where x_f^* indicates the front location of slower left-propagating current and t_s^* is chosen sufficiently large to ensure that the solution is quasisteady. For the faster-moving gravity current, we determine the effective height correspondingly by integrating over the x interval from the front of the faster-moving current to the front of the slower-moving current and finally the interfacial gravity current height can be computed by taking the integration over the x interval from $L_{\rm lock}^*$ to the front of this current. Figure 9 demonstrates that these effective current heights indeed approach quasisteady values. In order to compare the DNS results with predictions by the vorticity model, we employ the current heights at time $t_s^* = 50$, when they have reached quasisteady values.

The velocity U_b^* and height h_b^* of the right-propagating bore are evaluated as follows. As the bore propagates along the interface, it deflects this interface upward or downward, thereby causing a rapid change in $\partial\rho^*/\partial x^*$ along $y^* = d_l^*$. By starting at the right wall and sweeping leftward along $y^* = d_l^*$, we identify the x location where $\partial\rho^*/\partial x^*$ first exceeds 0.01 and take this as the location of the bore. Figure 10(a) shows the front location of the bore as a function of time, for the nonsymmetric case of Fig. 6. After a brief initial transient, we observe that the bore propagates with a constant velocity. It also validates that assuming a constant velocity for this instability and treating it like a bore is in agreement with the simulations.

From Eq. (42) we can evaluate the local interface height η_b^* as a function of time. We can then define the effective bore height h_b^* as the average height of the interface over the x interval from the bore front location $x_{f,c}^*$ to the interfacial gravity current nose $x_{f,b}^*$,

$$h_b^* = \frac{\int_{x_{f,c}^*}^{x_{f,b}^*} \eta_b^*(x^*,t_s^*)dx^*}{x_{f,b}^* - x_{f,c}^*}, \tag{44}$$

where we take $t_s^* = 50$ to ensure a quasisteady result, as indicated by Fig. 10(b). Regardless of the undular nature of this bore, the average height of the interface behind the bore reaches a constant value. The deflection in the interface height can be evaluated as

$$d^* = |h_b^* - d_l^*|. \tag{45}$$

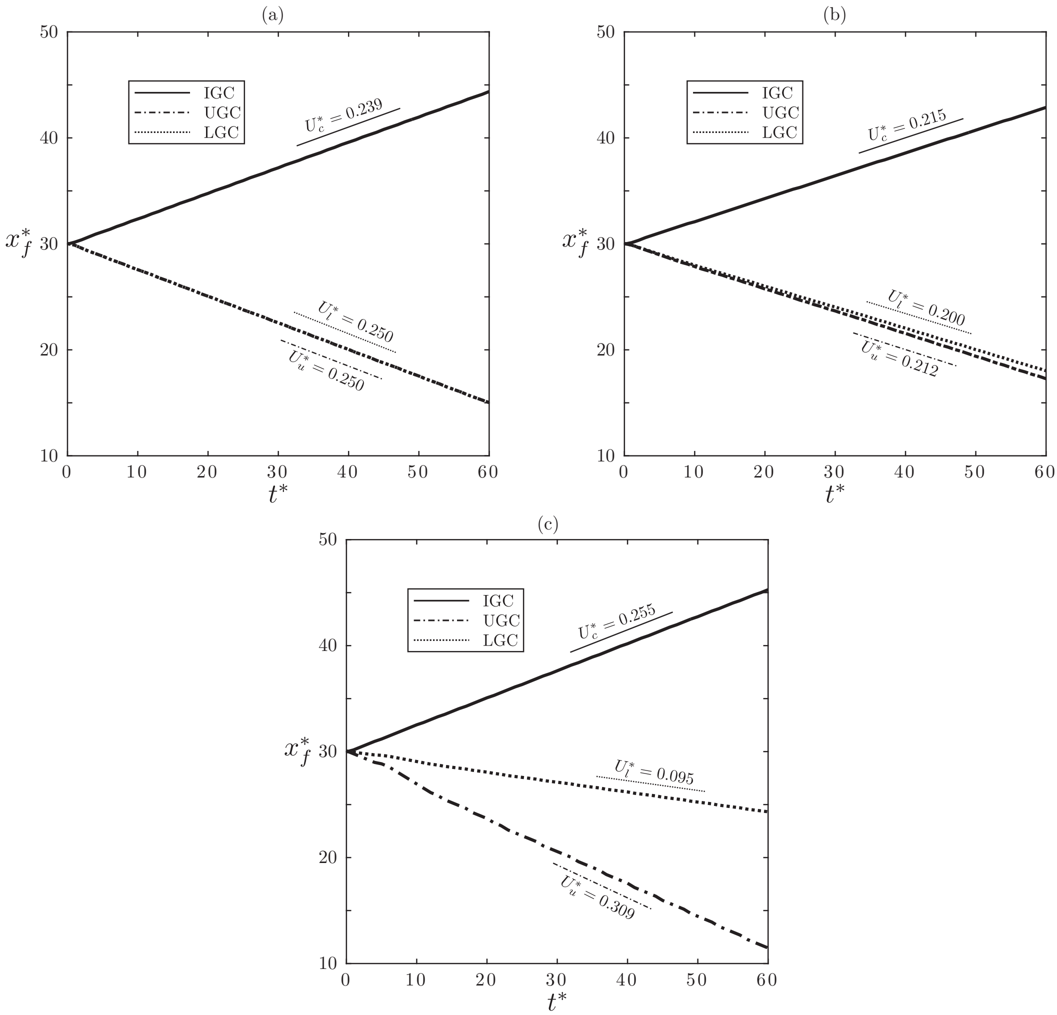

FIG. 8. Simulation results for the front locations as functions of time, for the flows shown in Figs. 4–6: (a) $\rho_c^* = d_l^* = 0.5$, (b) $\rho_c^* = d_l^* = 0.3$, and (c) $\rho_c^* = 0.5$ and $d_l^* = 0.3$. Here IGC stands for interfacial gravity current, while UGC and LGC denote upper gravity current and lower gravity current, respectively. The straight line segments represent the quasisteady front velocities, obtained by linear fits of the DNS results.

V. DISCUSSION OF RESULTS

In the following, we will discuss DNS results and compare them with predictions by the vorticity model and by earlier models of other authors, as well as with earlier experimental observations. For the equilibrium intrusion case, where $\rho_c^* = d_l^*$, the vorticity model predictions are based on the symmetric configuration of Fig. 1, while for nonequilibrium cases we employ the model 2 configuration, depicted by Fig. 3. We will also compare model 2 with model 1 at the end of this section. We note that in the limit of $d_l^* \to \rho_c^*$, the predictions for the nonsymmetric case smoothly approach those of the symmetric case for all physical variables. To discuss the physical results, we employ phase-space plots in the (ρ_c^*, d_l^*) plane. Figure 11(a) shows vorticity model predictions for the intrusion velocity U_c^*. For the case of a doubly symmetric intrusion with $\rho_c^* = d_l^* = 0.5$, the model predicts $U_c^* = 0.25$, which is consistent with the earlier results of [10,16] for energy-conserving currents, when rescaled for half the tank height. For the limiting cases of $(\rho_c^* = 0, d_l^* = 1)$ and

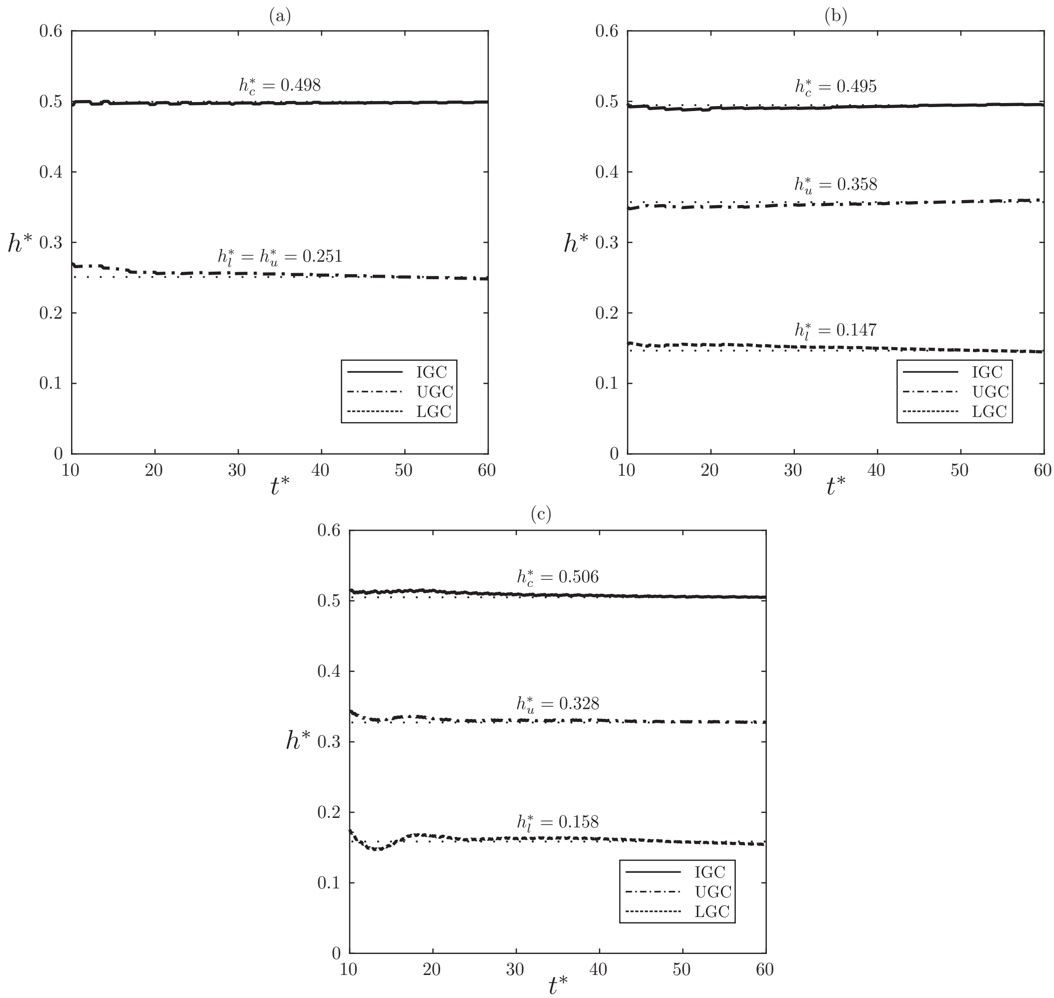

FIG. 9. Effective current heights h_l^* and h_u^* as functions of time, for the flows shown in Figs. 4–6: (a) $\rho_c^* = d_l^* = 0.5$, (b) $\rho_c^* = d_l^* = 0.3$, and (c) $\rho_c^* = 0.5$ and $d_l^* = 0.3$. The solid and dash-dotted lines indicate the instantaneous heights of the lower and upper gravity currents, respectively. The dotted horizontal lines indicate the quasisteady values evaluated at $t^* = 50$.

($\rho_c^* = 1, d_l^* = 0$) the model predicts front velocities near one-half, but not exactly equal to one-half. As we will see below, this reflects the fact that as $d_l^* \rightarrow 0$ or 1, the bore height does not approach zero. In other words, the limits of $d_l^* \rightarrow 0$ and 1 are singular, in the sense that the flow does not reduce to the case of a full-depth lock-release gravity in a smooth fashion. We remark that the doubly symmetric case represents a point of symmetry for the figure, so an intrusion with (ρ_c^*, d_l^*) has the same velocity as one with ($1 - \rho_c^*, 1 - d_l^*$). Recall that Cheong *et al.* [7] found that for a fixed value of d_l^* the intrusion speed does not depend on the intrusion density. The vorticity model shows that in the range $0.2 < \rho_c^* < 0.8$ the intrusion velocity indeed varies only weakly with the density. However, for very small or large intrusion densities, the intrusion speed depends more strongly on its density. Cheong *et al.* [7] had furthermore observed that for a fixed intrusion density, the equilibrium configuration has the minimum propagation velocity. This is confirmed by the contours of Fig. 11(a), which have their extrema along the main diagonal. Figure 11(b) shows corresponding results for the intrusion thickness h_c^*. Along the main diagonal $\rho_c^* = d_l^*$, we find that h_c^* has a constant value of 0.5,

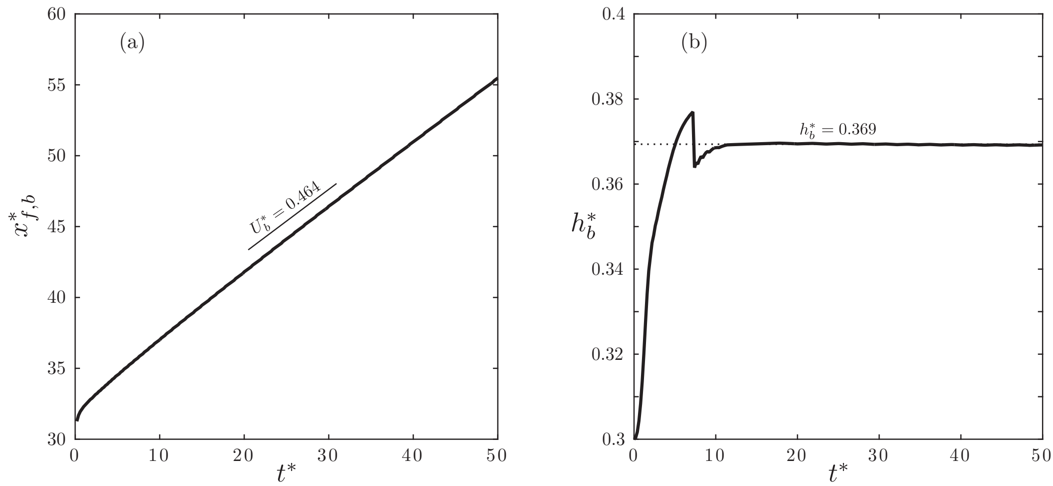

FIG. 10. Variation of the (a) front location and (b) height of the right-propagating internal bore as a function of time, for the nonsymmetric intrusion shown in Fig. 6.

which is consistent with the observation that for $\rho_c^* = d_l^*$ we obtain energy-conserving equilibrium intrusions. Away from the diagonal the intrusion thickness increases, which suggests that it is gaining energy. We will return to this point in Sec. VI.

Figure 12(a) shows the phase-plane diagram for the ratio U_b^*/U_c^* of the bore velocity to the intrusion velocity, while Fig. 12(b) presents corresponding results for the bore height. The bore height is seen to vanish along the diagonal $\rho_c^* = d_l^*$, consistent with the formation of equilibrium intrusions. As mentioned above, in the limit of $d_l^* \to 0$ or 1, the bore height does not approach zero, so the flow does not reduce to a full-depth lock-exchange gravity current in a smooth fashion.

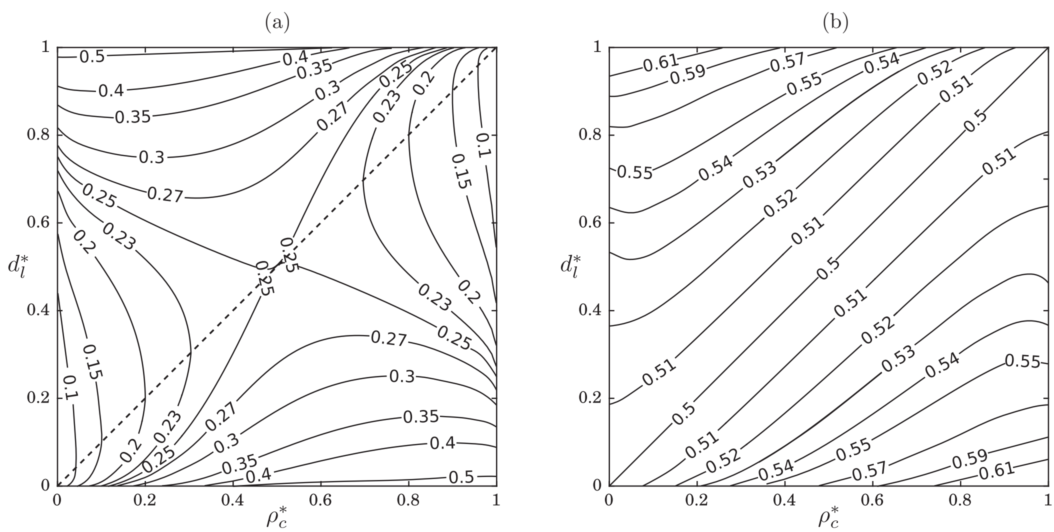

FIG. 11. Phase-space diagram for (a) the intrusion velocity U_c^* and (b) the intrusion thickness h_c^*. Equilibrium intrusions form along the diagonal $d_l^* = \rho_c^*$. For a given ρ_c^*, the minimum velocity is shown to occur for the equilibrium intrusion, located on the dashed diagonal line.

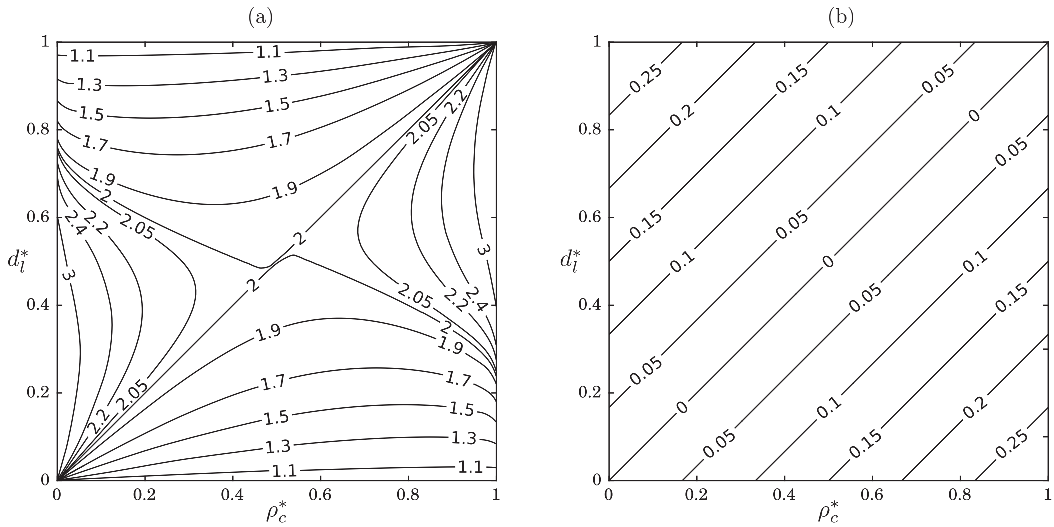

FIG. 12. (a) Phase-space diagram for the ratio of the leading bore speed to the intrusion speed U_b^*/U_c^*. For equilibrium intrusions $U_b^*/U_c^* = 2$, consistent with the value for linear long waves. (b) Phase-space diagram for the interfacial deflection d^* due to the leading bore. Here d^*, defined by Eq. (45), varies linearly with the magnitude of difference between ρ_c^* and d_l^*.

As pointed out in Refs. [6,8], in the limit of vanishing height bores travel with the speed of long waves, so $U_b^*/U_c^* \to 2$. This is confirmed by Fig. 12(a). Furthermore, in the limit of $d_l^* \to 0$ or 1, U_b^*/U_c^* barely exceeds one, so the intrusion moves almost as fast as the leading bore. We note that all contours in Fig. 12(b) are parallel to the main diagonal and equidistant, which suggests that the bore height depends only on the difference between ρ_c^* and d_l^* and this dependence is linear, as will be demonstrated more clearly, later in Fig. 17. This is consistent with earlier observations in Refs. [7,8]. We note that for the relation $d^* = \Lambda(\rho_c^* - d_l^*)$ the current model predicts approximately the same value of Λ as those earlier two investigations, which corroborates the assumptions made in those studies.

Figure 13 displays phase-plane results for the velocities and thicknesses of the left-propagating upper and lower gravity currents. For increasing ρ_c^* and decreasing d_l^* the bottom-propagating gravity current slows down, due to a decrease in its available potential energy. In fact, for large values of ρ_c^* and small values of d_l^* the bottom current can have a negative front velocity, so it travels to the right. Corresponding results are obtained for the top current. Note that for $d_l^* \approx 1$ and small ρ_c^* the vorticity model predicts values of the lower gravity current velocity $U_l^* > 0.8$. This is much larger than the value of one-half for a full-depth lock-exchange gravity current, which again indicates that the limits of $d_l^* \to 0$ and 1 are singular. This singularity may be a consequence of treating the interfacial disturbance as a bore, which may no longer be valid as we approach these limits. It furthermore suggests that in this limit the lower gravity current in the intrusion configuration is gaining energy. We will return to this issue below.

The behavior of the gravity current height contours is interesting as well. As demonstrated by Figs. 13(c) and 13(d), for a constant intrusion density, the isolines are approximately equidistant over a large range of d_l^*, which suggests a nearly linear variation of h_l^* and h_u^* with d_l^*. Again, the limit of $d_l^* \to 1$ is informative. For ρ_c^* values near one, the flow is near equilibrium, so no sizable bore forms and the upper ambient layer becomes dynamically unimportant. Hence the flow becomes similar to a traditional full-depth lock-exchange problem with current depths near one-half, although much smaller front velocities. On the other hand, for $d_l^* \to 1$ but ρ_c^* near zero, a large bore forms in the upper ambient layer and the lower gravity current thickness is reduced to about 0.35. We note that this problem has an inherent symmetry as a result of the Boussinesq approximation, in that there

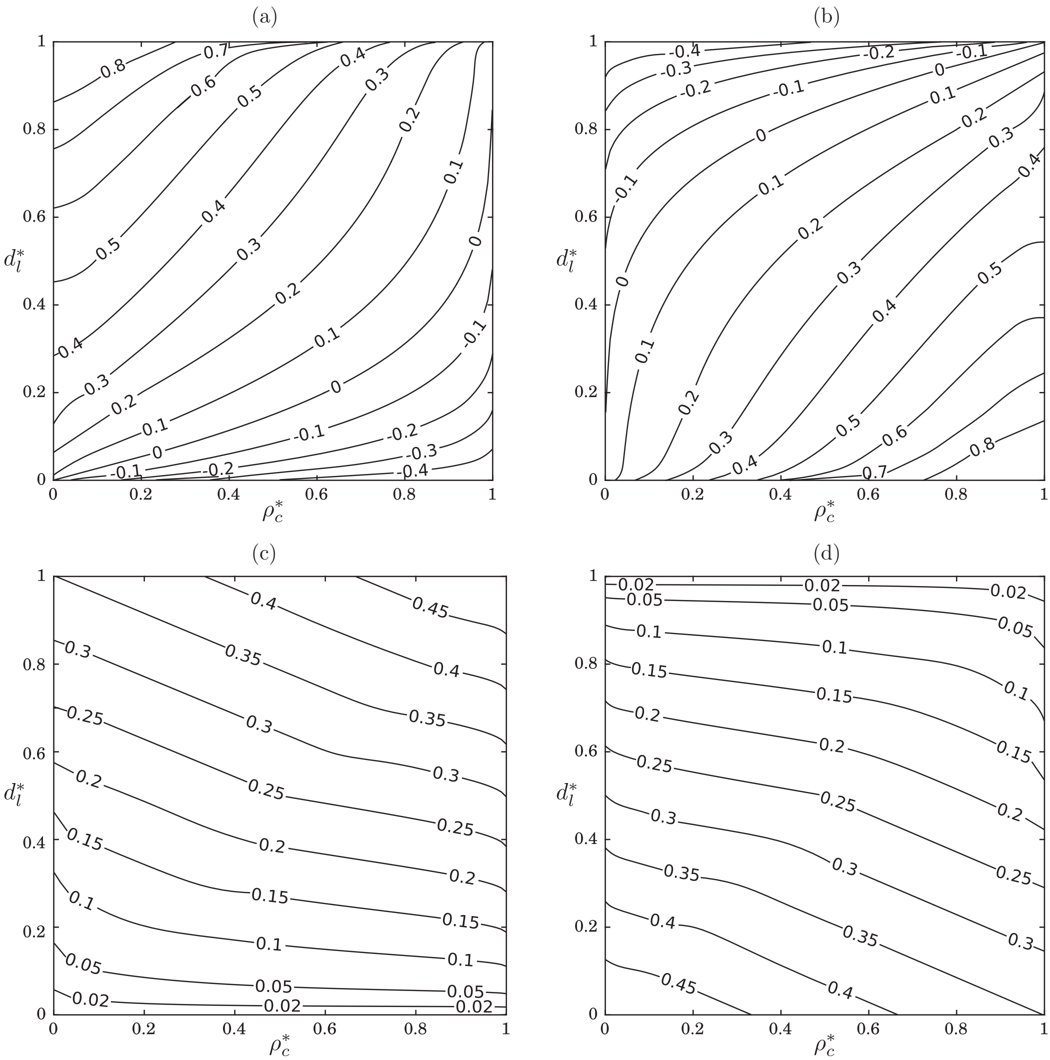

FIG. 13. Phase-space diagram for the velocities (a) U_l^* and (b) U_u^* and heights (c) h_l^* and (d) h_u^* of the lower and upper gravity currents. A discussion of the results is provided in the text.

is an equivalence between intrusions with ρ_c^* and d_l^* on the one hand and those with $1-\rho_c^*$ and d_l^* on the other. Consequently, the following expressions hold:

$$U_c^*(\rho_c^*,d_l^*) = U_c^*(1-\rho_c^*,1-d_l^*), \tag{46}$$

$$U_l^*(\rho_c^*,d_l^*) = U_u^*(1-\rho_c^*,1-d_l^*), \tag{47}$$

$$h_l^*(\rho_c^*,d_l^*) = h_u^*(1-\rho_c^*,1-d_l^*). \tag{48}$$

For the intrusion velocity, Fig. 14 compares vorticity model predictions with current DNS results, as well as with earlier experimental data and model predictions by other authors. Within the present investigation, we conducted simulations for $d_l^* = 0.1, 0.2, \ldots, 0.9$, as well as for the ρ_c^* values of 0.25, 0.5, and 0.61, in order to be able to compare with the earlier theoretical and experimental investigations of [7,8]. The figure shows that the vorticity model predictions are close to those

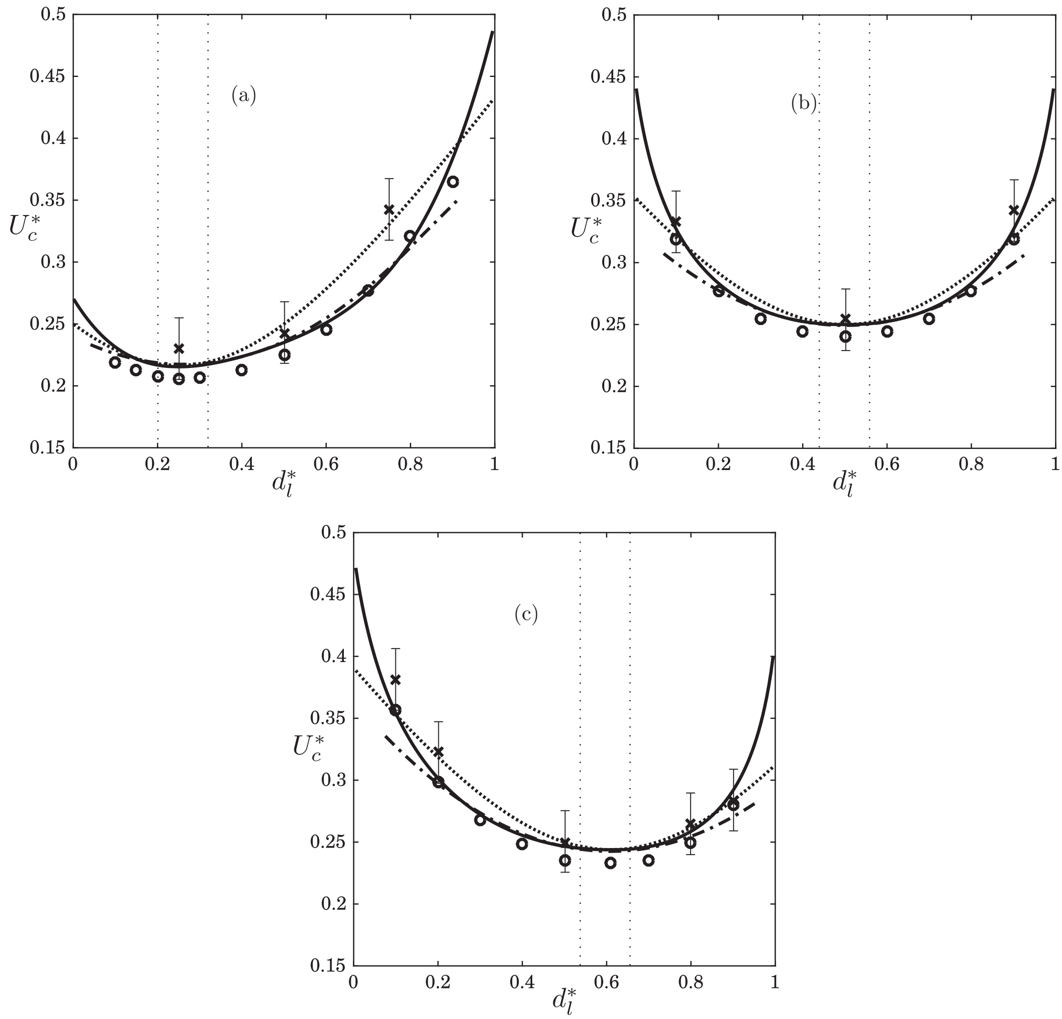

FIG. 14. Interfacial gravity current speed U_c^* as a function of the interface height d_l^*, for (a) $\rho_c^* = 0.25$, (b) $\rho_c^* = 0.50$, and (c) $\rho_c^* = 0.61$. Solid lines represent the present vorticity model predictions, dotted lines show the results of the global energy-conserving model proposed by [7], dash-dotted lines indicate the intrusion speed given by [8], and discrete circles and crosses represent the present DNS results and the experimental data of [7], respectively. The vertical dotted lines demonstrate the range of validity of the investigation by [5]. Within this range, their results (not shown here) agree closely with all other theoretical, numerical, and experimental data.

of the earlier models in Refs. [7,8] and over a substantial range of d_l^* fall in between these two models. Within its narrow range of validity between the vertical dotted lines, the model of [5] yields predictions in very close agreement with those of the other models, so we do not show them in this figure. All four models predict that the minimum propagation velocity occurs at equilibrium conditions, which is consistent with the experimental observations of [7] and the present simulation results. Due to the finite Re values employed in the DNSs, the DNS front velocity data generally fall slightly below the vorticity model predictions, as will be discussed in further detail below.

Figure 15 compares vorticity model predictions with DNS results for the intrusion thickness as a function of the interface height. For all three ρ_c^* values, h_c^* reaches a minimum value of 0.5 for

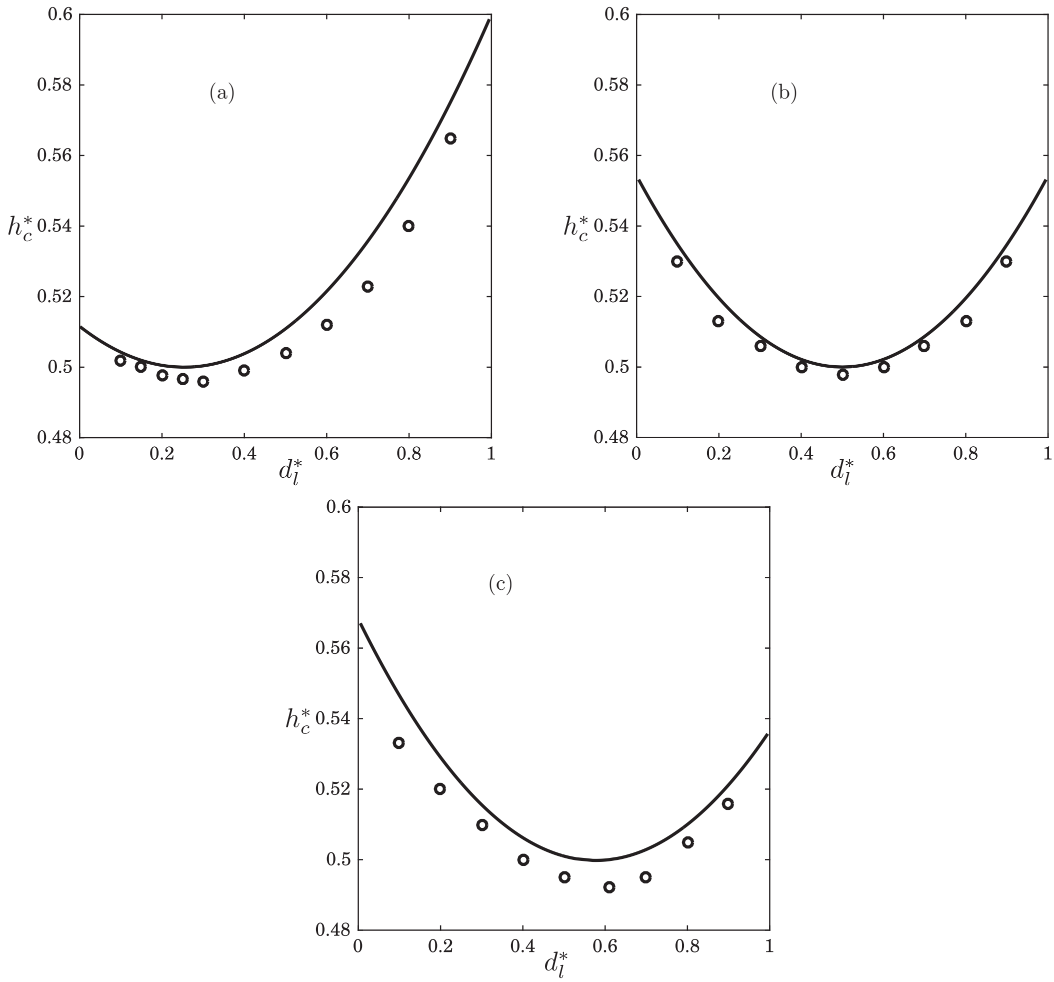

FIG. 15. Interfacial gravity current thickness h_c^* as a function of the interface height d_l^*, for (a) $\rho_c^* = 0.25$, (b) $\rho_c^* = 0.50$, and (c) $\rho_c^* = 0.61$. Solid lines indicate predictions by the present vorticity model, while discrete circles represent the present DNS results.

the equilibrium case. Away from the equilibrium point, the intrusion thickens. We will discuss this observation from an energy perspective in Sec. VI.

The DNSs show that the bore propagates with an approximately constant velocity. Figure 16 presents vorticity model predictions and simulation data for the ratio of the bore velocity to the intrusion velocity U_b^*/U_c^*, as a function of d_l^* and ρ_c^*. As explained in Ref. [8], in the limiting case where the bore height $d^* \to 0$, U_b^* approaches the linear long wave speed $\sqrt{d_l^* d_u^*}$. Hence, for near-equilibrium intrusions we expect that $U_b^*/U_c^* \to 2$, which is confirmed by the vorticity model predictions and DNS results.

Figure 17 shows the dimensionless bore amplitude d^* as a function of the interface height d_l^* for the same three ρ_c^* values. Due to the undular nature of this leading bore, d^* is evaluated as a spatial average of the interface height. The present vorticity model predictions are shown to be in close agreement with the results of [8]. Specifically, both models exhibit a linear dependence of the bore height on $|\rho_c^* - d_l^*|$. Hence the vorticity model provides theoretical support for the empirical assumptions underlying Eq. (4.16) of [8]. Figure 18 demonstrates that both model predictions are consistent with corresponding DNS results.

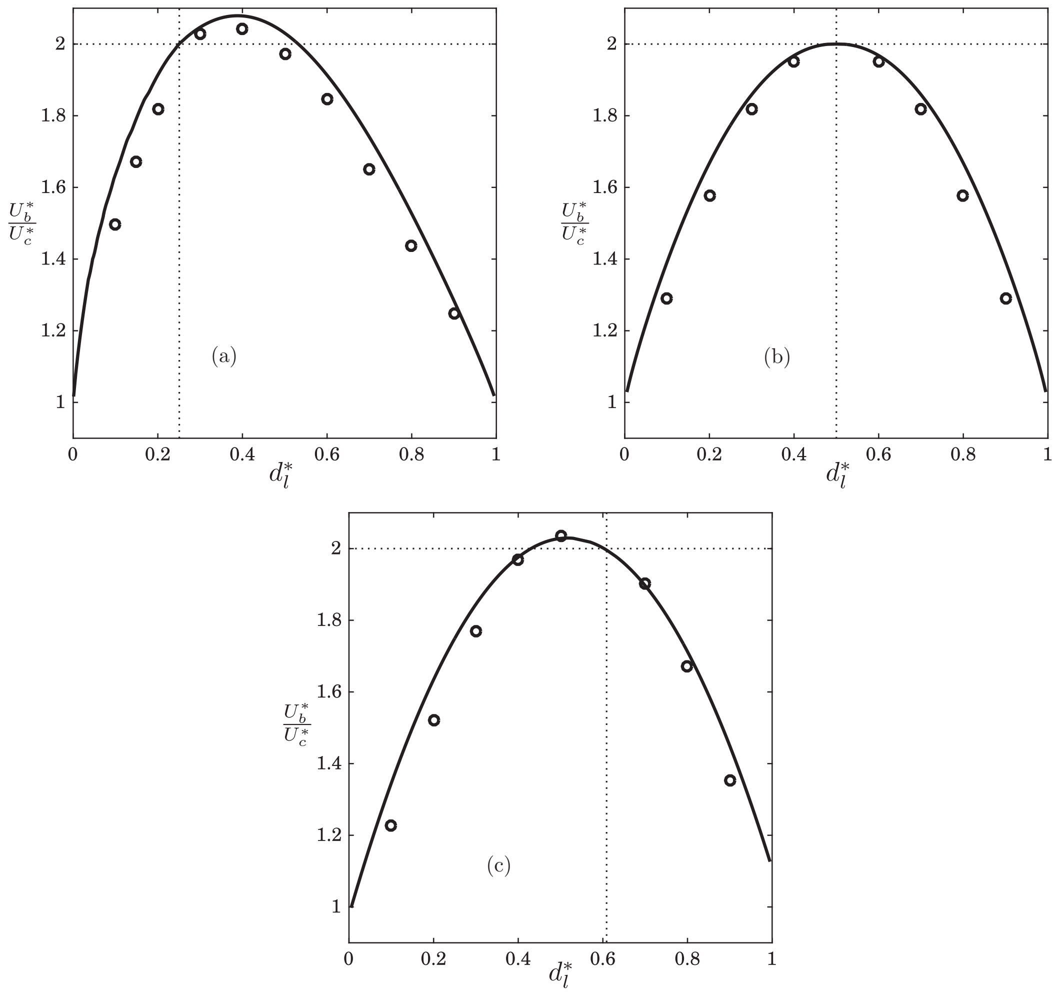

FIG. 16. Variation of the ratio of leading bore speed to intrusion speed U_b^*/U_c^* with interface height d_l^*, for (a) $\rho_c^* = 0.25$, (b) $\rho_c^* = 0.50$, and (c) $\rho_c^* = 0.61$. Solid lines represent the present vorticity model predictions, while discrete circles indicate the present DNS results. The dotted lines show that for $d_l^* = \rho_c^*$ the model predicts $U_b^*/U_c^* = 2$, as expected for linear waves.

For the propagation velocities of the upper and lower gravity currents, Fig. 19 compares the vorticity model predictions to the DNS results. Again, good overall agreement is observed. The velocity of each gravity current is a function of its available potential energy, which scales with the square of the layer height multiplied by its density difference relative to the intrusion fluid. Both the model predictions and the DNS results confirm that under equilibrium conditions ($\rho_c^* = d_l^*$) the gravity currents have identical front velocities. When $d_l^* < \rho_c^*$, the lower gravity current has less available energy than the upper one, so it travels more slowly. As d_l^* increases, the lower gravity current speeds up while the upper one slows down, until for $d_l^* = \rho_c^*$ the two velocities become equal to each other. Beyond this point, the lower gravity current propagates faster than the upper one.

We now proceed to discuss results for the quasisteady current heights. Figure 20 compares the DNS values for the lower and upper current heights with the corresponding vorticity model predictions. Again, good agreement between the model predictions and the simulation results is observed over the entire range of d_l^*, for all three values of ρ_c^*. Moreover, as demonstrated by this figure, h_l^* and h_u^* vary nearly linearly with the interface height, especially far from $d_l^* = 0$ or $d_l^* = 1$.

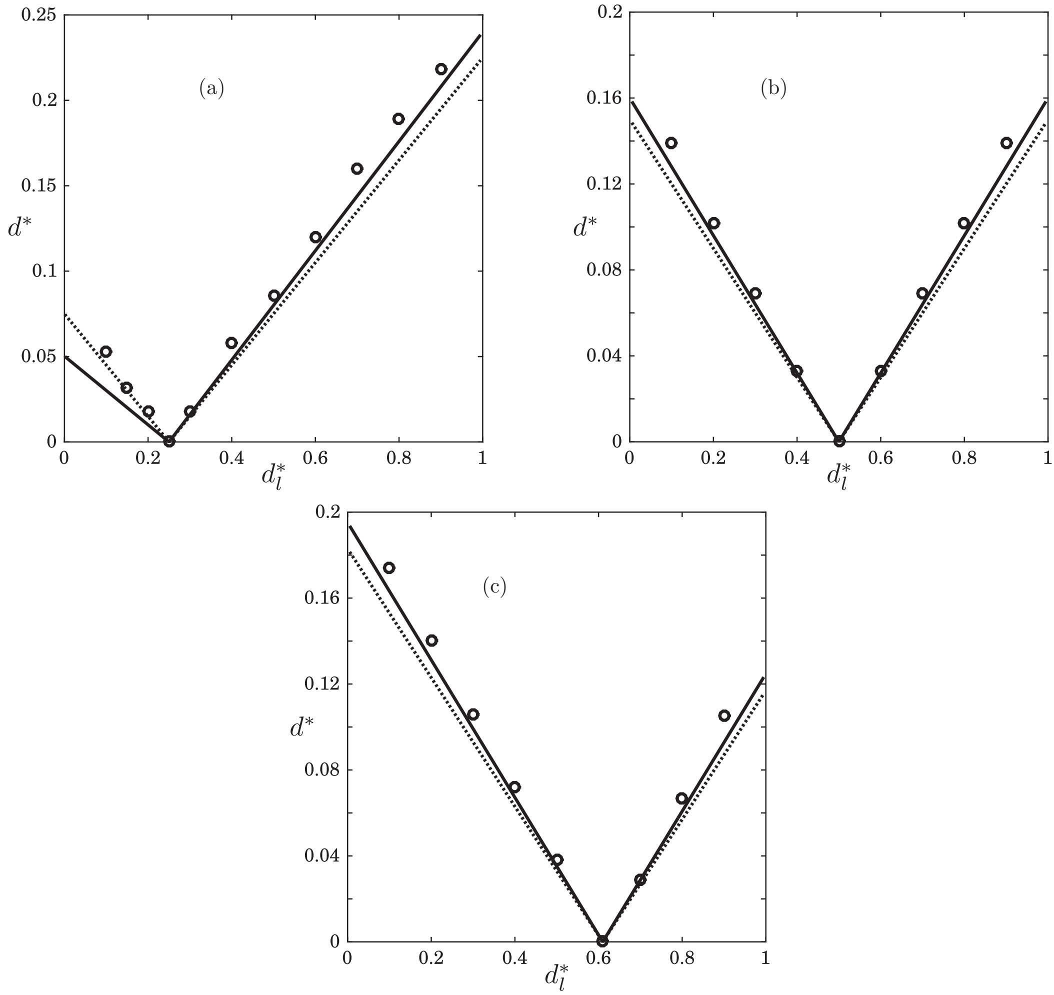

FIG. 17. Variation of the amplitude d^* of the right-propagating internal bore with the interface height d_l^*, for (a) $\rho_c^* = 0.25$, (b) $\rho_c^* = 0.50$, and (c) $\rho_c^* = 0.61$. The solid lines represent the present vorticity model predictions, the dotted lines show results of [8], and the discrete circles indicate the present DNS results.

The slopes of the curves are close to 0.5 (and −0.5 for h_u^*), for all values of ρ_c^*. Recall that for equilibrium intrusions we had found $h_l^* = d_l^*/2$ and $h_u^* = d_u^*/2$.

For $\rho_c^* = 0.5$ and the entire range of d_l^*, Fig. 21 compares predictions by the simplified model 1 (Fig. 2) with those of the more complete model 2 (Fig. 3), which accounts for the bore in the faster moving gravity current. We observe that the predictions by the two different models are close to each other, as well as to the simulation results, for the intrusion velocity, the gravity current heights, and the ratio of the right-propagating bore velocity to the intrusion velocity. On the other hand, for the velocity of the faster left-propagating current, which accounts for the key difference between the two models, the two model predictions deviate substantially from each other and the more comprehensive model 2 yields closer agreement with the DNS results.

VI. ENERGY DISCUSSION

All of the above information about the flow was gained without any consideration of energy arguments. This is in contrast to all earlier analyses of intrusion current models, which had invoked

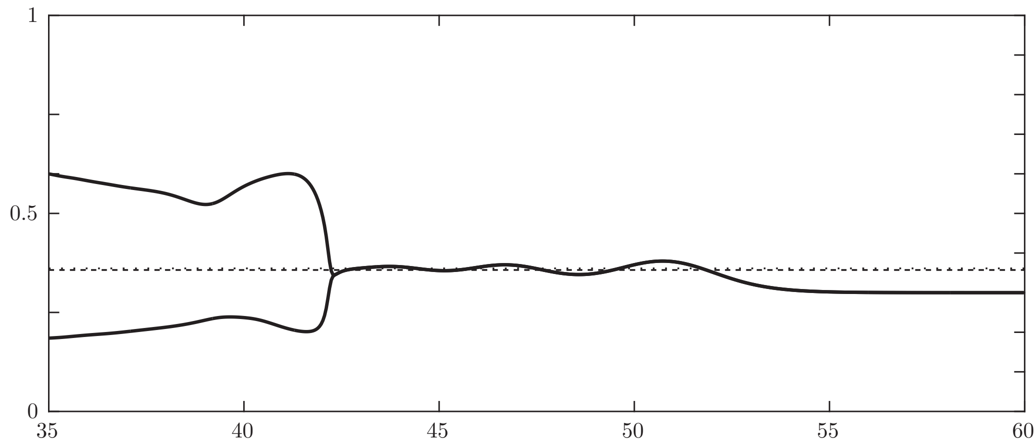

FIG. 18. Comparison between the present DNS results and model predictions for the bore height, i.e., the height of the interface between the intrusion front and the leading bore. The dashed and dotted horizontal lines, which are nearly identical, indicate the predictions by the present vorticity model and that of [8] for h_b^*, respectively. The DNS results (solid line) represent the interface location from the nonequilibrium simulation in Fig. 6 at $t^* = 50$, for $\rho_c^* = 0.5$ and $d_l^* = 0.3$. The bore is undular in nature and the DNS interface height fluctuates around an average value that is closely approximated by the dashed and dotted horizontal lines. We take this as an indication of good agreement between the model predictions and the simulation results.

energy-related assumptions in certain parts of the flow field. Consequently, we can now investigate the energy balance along certain streamlines and in specific control volumes a *posteriori*, in order to obtain insight into the validity of the assumptions underlying earlier models. Toward this objective, we analyze the head loss along the bottom and top of the tank, denoted by Δ_l and Δ_u, from D to C and G to I, in the control volume $CDGI$ and in the reference frame of the interfacial gravity current, shown in Fig. 3. We furthermore calculate the head loss inside the intrusion, indicated by Δ_c, from B' to C', along the streamline passing through these two points in the control volume of $BCIJ$. We consider the following modified Bernoulli equations in which we allow for an energy loss or gain to occur:

$$p_G + \tfrac{1}{2}\rho_{\text{ref}}(U_c + U_{ub})^2 = p_I + \tfrac{1}{2}\rho_{\text{ref}}(U_c + U_u')^2 + \Delta_u, \tag{49}$$

$$p_D + \tfrac{1}{2}\rho_{\text{ref}}(U_c - U_{lb})^2 = p_C + \tfrac{1}{2}\rho_{\text{ref}}(U_c + U_l)^2 + \Delta_l, \tag{50}$$

$$p_{B'} + \tfrac{1}{2}\rho_{\text{ref}}(U_l + U_{bc})^2 = p_{C'} + \tfrac{1}{2}\rho_{\text{ref}}(U_l + U_c)^2 + \Delta_c. \tag{51}$$

Here $p_{()}$ denotes the pressure at the corresponding location. In Eqs. (49)–(51) the velocities are known from the earlier analysis presented in Secs. II and III. The required pressure differences, in the absence of viscous forces along the top and bottom boundaries, can readily be obtained from the horizontal-momentum-conservation equations for the respective control volumes, which have the general form

$$\int (p_i + \rho_{\text{ref}}U_i^2)dy = \int (p_o + \rho_{\text{ref}}U_o^2)dy, \tag{52}$$

where $\rho_{\text{ref}} = \rho_c$, consistent with the Boussinesq approximation, and i and o indicate inlet and outlet, respectively. By assuming that the pressure is hydrostatic at the inflow and outflow boundaries of the respective control volumes, i.e., far from any front so that the flow is locally unidirectional, we

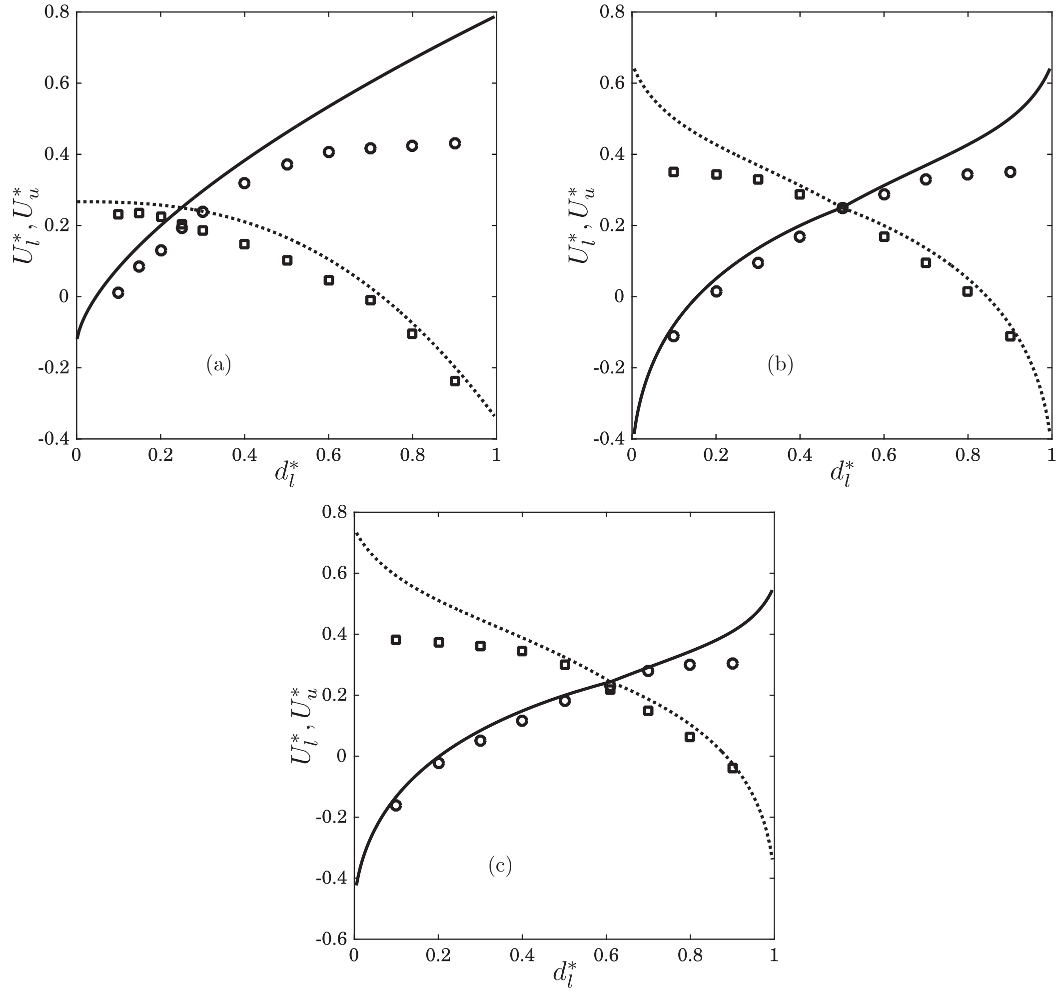

FIG. 19. Front velocities U_l^* and U_u^* of the left-propagating lower and upper gravity currents, as functions of the interface height d_l^*, for (a) $\rho_c^* = 0.25$, (b) $\rho_c^* = 0.50$, and (c) $\rho_c^* = 0.61$. In this figure, solid and dotted lines represent model-predicted values of lower and upper gravity currents, respectively, while discrete circles and squares are the respective simulation speeds of these two gravity currents.

obtain the following dimensionless expressions for the corresponding pressure drops:

$$p_G^* - p_I^* = \frac{(U_c^* + U_u'^*)^2 h_u'^* - (U_c^* + U_{ub}^*)^2(1 - h_b^*) + \frac{1}{2}\rho_c^*(1 - h_b^* - h_u'^*)^2}{1 - h_b^*}, \tag{53}$$

$$p_D^* - p_C^* = \frac{(U_c^* + U_l^*)^2 h_l^* - (U_c^* - U_{lb}^*)^2 h_b^* + \frac{1}{2}(1 - \rho_c^*)(h_b^* - h_l^*)^2}{h_b^*}, \tag{54}$$

$$p_{B'}^* - p_{C'}^* = \frac{(U_c^* + U_l^*)^2(h_b^* - h_l^*) - (U_{bc}^* + U_l^*)^2 h_b^* + \frac{1}{2}(1 - \rho_c^*)h_l^{*2}}{h_b^*}. \tag{55}$$

We note that pressure and head loss are nondimensionalized by $p_{\rm ref} = \Delta_{\rm ref} = \rho_c g' H$. All other variables are scaled according to Eqs. (12)–(14). By substituting Eqs. (53)–(55) into Eqs. (49)–(51), we obtain the desired head losses, as shown in the phase-space diagrams of Fig. 22. The figure confirms that all head losses vanish for $\rho_c^* = d_l^*$, i.e., for equilibrium intrusions. For all other

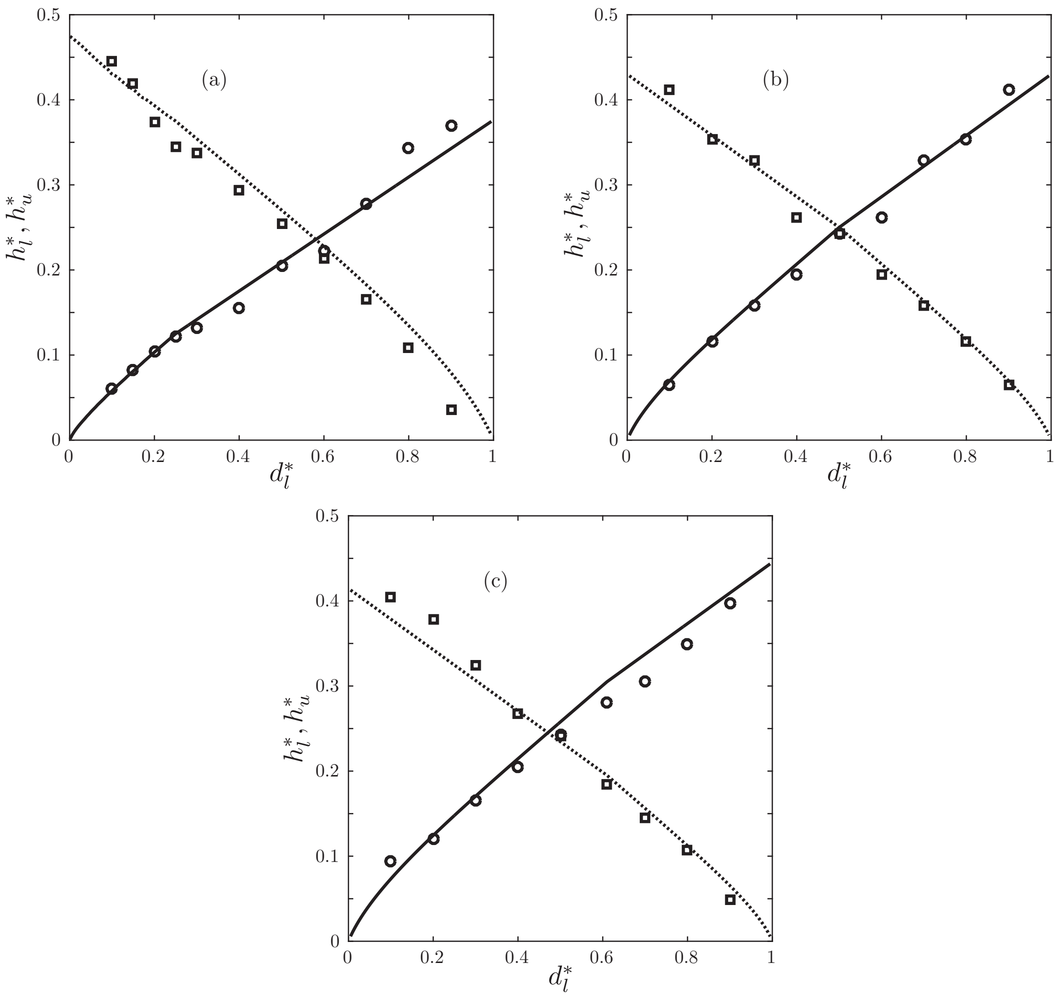

FIG. 20. Thicknesses h_l^* and h_u^* of the lower and upper and gravity currents, as functions of the interface height d_l^*, for (a) $\rho_c^* = 0.25$, (b) $\rho_c^* = 0.50$, and (c) $\rho_c^* = 0.61$. Solid and dotted lines represent the present vorticity model predictions for the lower and upper gravity currents, respectively. Discrete circles and squares indicate the corresponding DNS results. All of the DNS results were evaluated at $t_s^* = 50$.

situations, the head-loss terms are nonzero for all three currents. Furthermore, the head-loss contours again reflect the symmetry properties observed in the earlier analysis, so

$$\Delta_c^*(\rho_c^*, d_l^*) = \Delta_c^*(1 - \rho_c^*, 1 - d_l^*), \tag{56}$$

$$\Delta_l^*(\rho_c^*, d_l^*) = \Delta_u^*(1 - \rho_c^*, 1 - d_l^*). \tag{57}$$

Interestingly, we find that all nonequilibrium intrusions experience an energy *gain*. This is consistent with our earlier findings, shown in Figs. 15 and 11(b), that $h_c^* > 0.5$ for all nonequilibrium intrusions. Furthermore, the figure indicates that the left-propagating gravity currents can also gain energy for certain parameter ranges. The lower gravity current gains energy when $d_l^* > \rho_c^*$, while the upper gravity current experiences an energy gain when $d_l^* < \rho_c^*$. We expect that an energy gain of the lower current should result in an effective thickness of this current larger than one-half, i.e., $h_l^*/h_b^* > 0.5$. This is confirmed by Fig. 23.

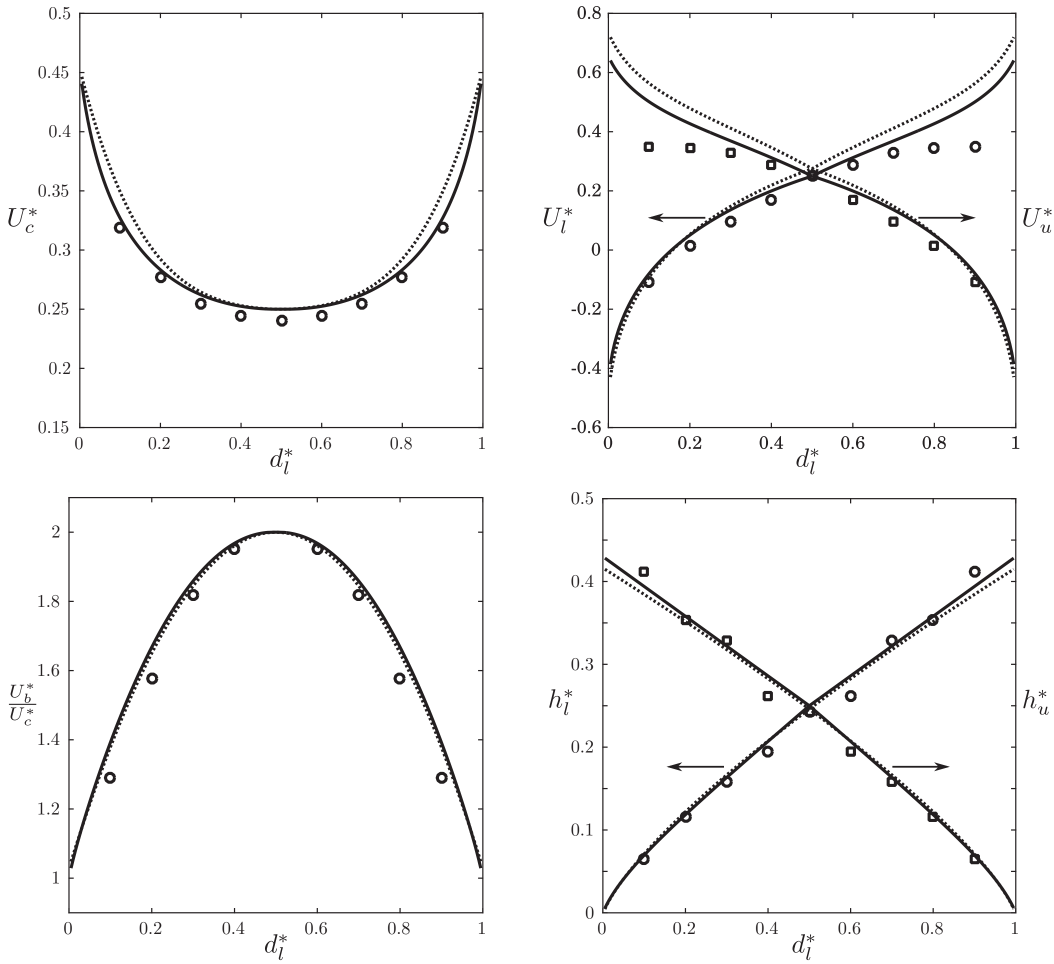

FIG. 21. Comparison of the predictions by the two nonsymmetric intrusion models proposed in Sec. III for the intrusion speed U_c^*, the lower and upper gravity currents speeds U_l^* and U_u^*, the ratio of leading bore speed to intrusion speed $\frac{U_b^*}{U_c^*}$, and the lower and upper gravity currents heights h_l^* and h_u^*. Solid lines indicate the results predicted by model 2, while dotted lines represent the results obtained by the simplified model 1. Discrete circles and squares show the numerical results. For all graphs, $\rho_c^* = 0.5$.

We now focus on the conversion of potential energy (PE) to kinetic energy (KE). Initially, when the fluid is at rest, all of the mechanical energy is in the form of PE. In the absence of any mixing, the theoretically lowest level of PE that can be achieved by the system corresponds to the state in which the dense, intermediate, and light fluids are arranged on top of each other in horizontal layers of thicknesses $(1-\alpha)d_l$, αH, and $(1-\alpha)(H-d_l)$, respectively, where α denotes the geometric ratio of L_{lock}/L. We can compute the PE per unit width of the initial state and of the final state of lowest energy, with respect to the bottom wall as

$$E_{p,i} = \tfrac{1}{2} g L \big\{\alpha\rho_c H^2 + (1-\alpha)\big[\big(\rho_l - \rho_u\big)d_l^2 + \rho_u H^2\big]\big\}, \tag{58}$$

$$E_{p,f} = \tfrac{1}{2} g L\{(\rho_l - \rho_c)[(1-\alpha)d_l]^2 + (\rho_c - \rho_u)[(1-\alpha)d_l + \alpha H]^2 + \rho_u H^2\}. \tag{59}$$

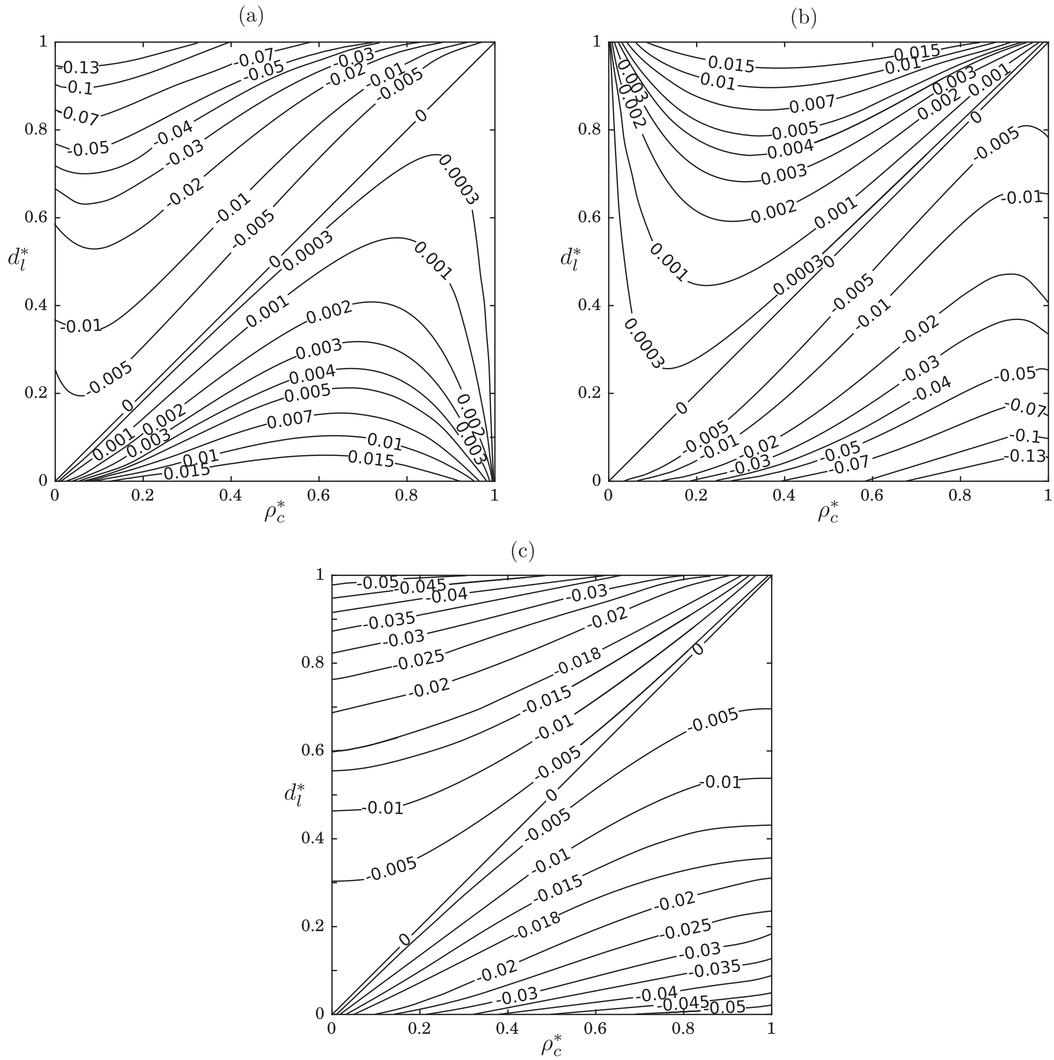

FIG. 22. Phase-space diagram for head loss along the (a) bottom (Δ_l^*), (b) top (Δ_u^*) and (c) centerline of intrusion (Δ_c^*), computed as functions of ρ_c^* and d_l^*.

The available potential energy $\mathcal{E}$ per unit width represents the difference between these two states

$$\mathcal{E} \;=\tfrac{1}{2} g L_{\text{lock}}(1-\alpha)\big[d_l^2\rho_l + (H^2 - 2d_l H)\rho_c + \big(-H^2 + 2d_l H - d_l^2\big)\rho_u\big], \tag{60}$$

We nondimensionalize the energy per unit width by $\rho_{\text{ref}} U_{\text{ref}}^3 x_{\text{ref}} t_{\text{ref}}$, which can be simplified to $\rho_c g' H^3$. We thus obtain

$$\mathcal{E}^* = \tfrac{1}{2}\beta(1-\alpha)\big(d_l^{*2} - 2d_l^*\rho_c^* + \rho_c^*\big), \tag{61}$$

where β indicates the ratio of the lock length to the tank height. As expected, $\mathcal{E}^*$ has a minimum with respect to d_l^* when $d_l^* = \rho_c^*$, which is consistent with our earlier observation that for a given value of ρ_c^* symmetric intrusions have the lowest propagation speed.

Once the gate is removed, PE is converted into KE. We can now employ the quasisteady front velocities calculated above from arguments of mass and momentum conservation, in order to calculate the rates at which the PE and KE of the overall flow, or of the various control volumes

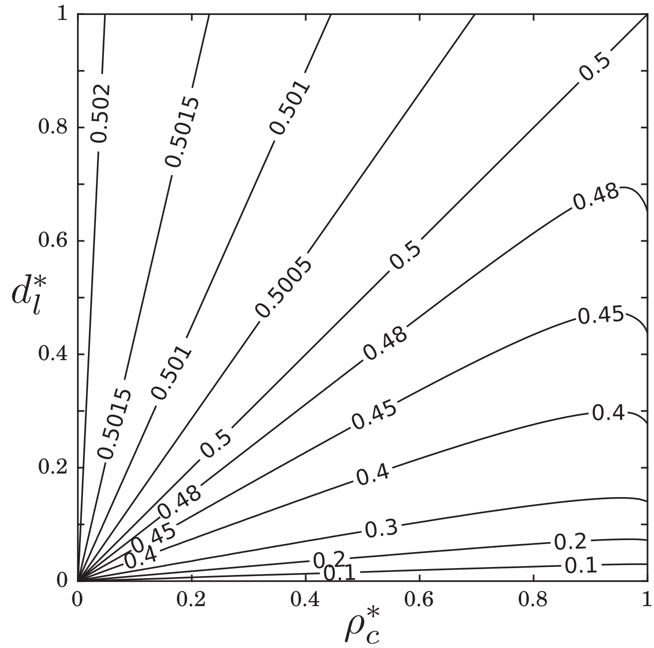

FIG. 23. Phase-space diagram for the ratio of the lower gravity current thickness h_l^* to the lower ambient current thickness h_b^* upstream of the intrusion. In the region where $d_l^* > \rho_c^*$, i.e., where the lower gravity current gains energy, this ratio exceeds one-half.

within the flow, change with time. For the symmetric intrusion case shown in Fig. 1, we can consider the entire tank as our control volume and evaluate the rate of change in KE and PE of the whole flow field, caused by the propagation of gravity currents. By multiplying the rate at which the area of each current grows with the kinetic energy per area, we obtain the respective rates at which KE of the individual currents grow

$$\dot{E}_{k,c} = \tfrac{1}{2}\rho_c(U_l + U_c)h_c U_c^2, \tag{62}$$

$$\dot{E}_{k,u} = \tfrac{1}{2}\rho_c(U_u + U_c)h_u U_u^2, \tag{63}$$

$$\dot{E}_{k,l} = \tfrac{1}{2}\rho_c(U_l + U_c)h_l U_l^2. \tag{64}$$

Here $\dot{E}_{k,c}$, $\dot{E}_{k,u}$, and $\dot{E}_{k,l}$ refer to the kinetic energies of the interfacial gravity current and of the left-propagating upper and lower currents, respectively. Note that as a result of the Boussinesq approximation, the density is taken as ρ_c for all currents. Nondimensionalizing the energy transfer rates by $\rho_{\text{ref}} U_{\text{ref}}^3 x_{\text{ref}}$ yields

$$\dot{E}_{k,c}^* = \tfrac{1}{2}(U_l^* + U_c^*)h_c^* U_c^{*2}, \tag{65}$$

$$\dot{E}_{k,u}^* = \tfrac{1}{2}(U_u^* + U_c^*)h_u^* U_u^{*2}, \tag{66}$$

$$\dot{E}_{k,l}^* = \tfrac{1}{2}(U_l^* + U_c^*)h_l^* U_l^{*2}. \tag{67}$$

By summing up the above expressions, we obtain that the rate of growth of KE in the entire flow field equals U_c^{*3}.

The rate at which PE of the entire tank changes can similarly be obtained by evaluating the rates at which fluid of one density is replaced by fluid of another density, via the motion of the individual currents. We obtain

$$\dot{E}_{p,c} = \tfrac{1}{2}(\rho_c - \rho_l)g\big(d_l^2 - h_l^2\big)U_c + \tfrac{1}{2}(\rho_c - \rho_u)g\big[(h_c + h_l)^2 - d_l^2\big]U_c, \tag{68}$$

$$\dot{E}_{p,u} = \tfrac{1}{2}(\rho_u - \rho_c)g[H^2 - (H - h_u)^2]U_u, \tag{69}$$

$$\dot{E}_{p,l} = \tfrac{1}{2}(\rho_l - \rho_c)gh_l^2U_l. \tag{70}$$

Rendering these results dimensionless gives

$$\dot{E}^*_{p,c} = -\tfrac{1}{2}(1 - \rho_c^*)\big(d_l^{*2} - h_l^{*2}\big)U_c^* + \tfrac{1}{2}\rho_c^*\big[(h_c^* + h_l^*)^2 - d_l^{*2}\big]U_c^*, \tag{71}$$

$$\dot{E}^*_{p,u} = -\tfrac{1}{2}\rho_c^*[1 - (1 - h_u^*)^2]U_u^*, \tag{72}$$

$$\dot{E}^*_{p,l} = \tfrac{1}{2}(1 - \rho_c^*)h_l^{*2}U_l^*. \tag{73}$$

Summing up expressions (71)–(73) yields that the flow field loses PE at the rate $-U_c^{*3}$, so that for symmetric intrusions indeed all of the lost potential energy is converted into kinetic energy. Alternatively, we can consider separately the control volumes above and below $y^* = d_l^*$, along the entire length of the tank. It is straightforward to show that the total energies inside each of these control volumes do not vary with time, which is consistent with our earlier observation that $\Delta_c^* = \Delta_l^* = \Delta_u^* = 0$ for symmetric intrusions.

In the following, we extend the analysis to nonsymmetric intrusions. We evaluate the rates at which PE and KE change for the intrusion and the lower and upper gravity currents, by focusing on the control volumes $BDGJ$, $B'D'GJ$, and $BDD'B'$ in the laboratory reference frame, as shown in Fig. 3. We obtain the rates of change of KE for the intrusion and the upper and lower currents as

$$\dot{E}_{k,c} = \tfrac{1}{2}\rho_c(U_l + U_c)h_cU_c^2 - \tfrac{1}{2}\rho_cU_l(H - h_u)U_{bc}^2, \tag{74}$$

$$\dot{E}_{k,u} = \tfrac{1}{2}\rho_c(U_l + U_c)h_u'U_u'^2 - \tfrac{1}{2}\rho_cU_lh_uU_u^2 - \tfrac{1}{2}\rho_cU_cU_{ub}^2(H - h_b), \tag{75}$$

$$\dot{E}_{k,l} = \tfrac{1}{2}\rho_c(U_l + U_c)h_lU_l^2 - \tfrac{1}{2}\rho_cU_ch_bU_{lb}^2. \tag{76}$$

Rendering the above equations nondimensional yields

$$\dot{E}^*_{k,c} = \tfrac{1}{2}(U_l^* + U_c^*)h_c^*U_c^{*2} - \tfrac{1}{2}U_l^*(1 - h_u^*)U_{bc}^{*\,2}, \tag{77}$$

$$\dot{E}^*_{k,u} = \tfrac{1}{2}(U_l^* + U_c^*)h_u'^*U_u'^{*2} - \tfrac{1}{2}U_l^*h_u^*U_u^{*2} - \tfrac{1}{2}U_c^*U_{ub}^{*2}(1 - h_b^*), \tag{78}$$

$$\dot{E}^*_{k,l} = \tfrac{1}{2}(U_l^* + U_c^*)h_l^*U_l^{*2} - \tfrac{1}{2}U_c^*h_b^*U_{lb}^{*\,2}. \tag{79}$$

By following the same approach as for symmetric intrusions, we find the rates of change of PE as a result of the current motion

$$\dot{E}_{p,c} = \tfrac{1}{2}(\rho_c - \rho_u)g\big[(h_l + h_c)^2 - h_b^2\big]U_c + \tfrac{1}{2}(\rho_c - \rho_l)g\big(h_b^2 - h_l^2\big)U_c, \tag{80}$$

$$\dot{E}_{p,u} = \tfrac{1}{2}(\rho_u - \rho_c)g[(H - h_u)^2 - (H - h_u')^2]U_l, \tag{81}$$

$$\dot{E}_{p,l} = \tfrac{1}{2}(\rho_l - \rho_c)gh_l^2U_l. \tag{82}$$

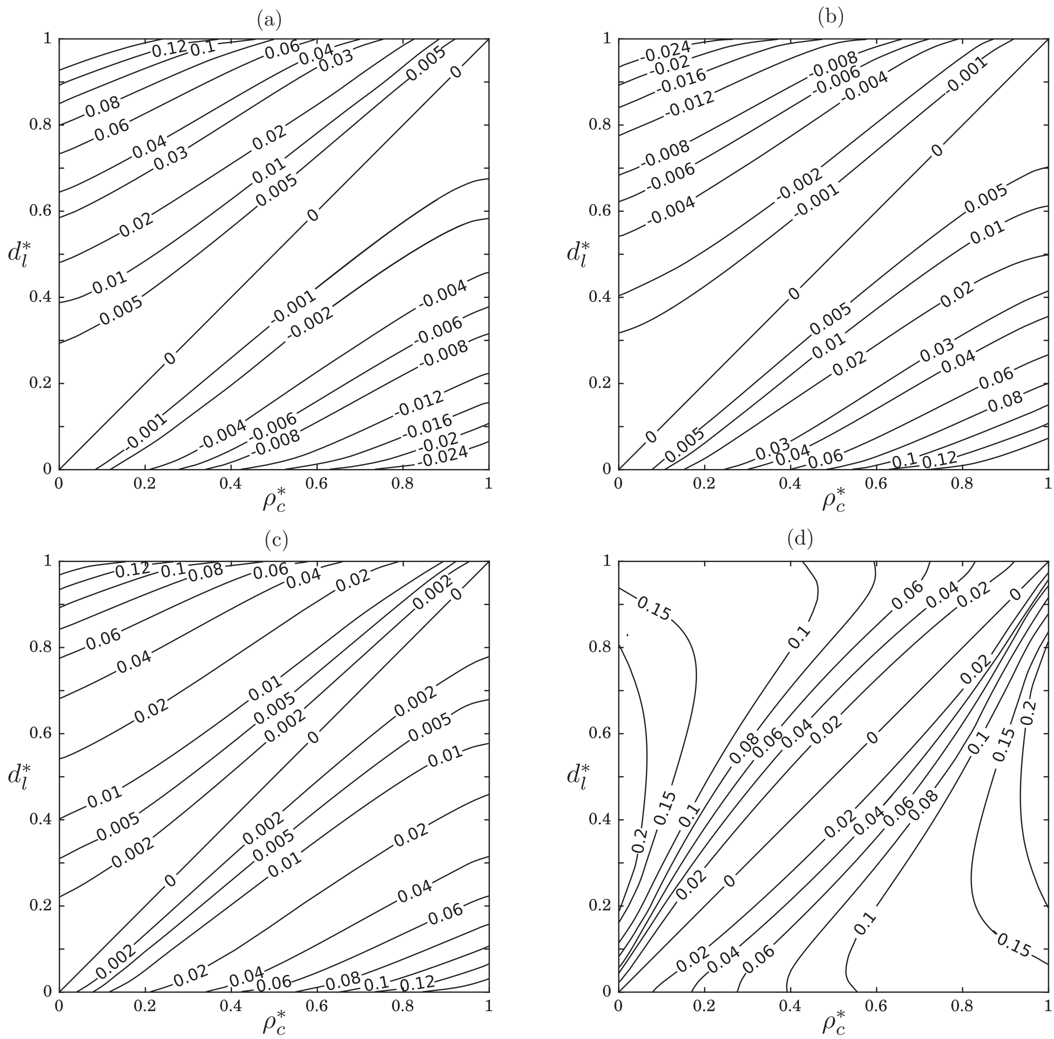

FIG. 24. Phase-space diagrams for the rates at which the mechanical energy changes with time inside the various control volumes: (a) $\dot{E}^*_{BDD'B'}$, (b) $\dot{E}^*_{B'D'GJ}$, and (c) $\dot{E}^*_{BDGJ}$. (d) Fraction of the potential energy released in control volume $ADGK$ that goes into the leading bore $|\dot{E}^*_b/\dot{E}^*_{p,ADGK}|$.

In dimensionless form, Eqs. (80)–(82) result in

$$\dot{E}^*_{p,c} = \tfrac{1}{2}\rho^*_c[(h^*_l + h^*_c)^2 - h^{*2}_b]U^*_c - \tfrac{1}{2}(1-\rho^*_c)\big(h^{*2}_b - h^{*2}_l\big)U^*_c, \tag{83}$$

$$\dot{E}^*_{p,u} = -\tfrac{1}{2}\rho^*_c[(1-h^*_u)^2 - (1-h'^*_u)^2]U^*_l, \tag{84}$$

$$\dot{E}^*_{p,l} = \tfrac{1}{2}(1-\rho^*_c)h^{*2}_l U^*_l. \tag{85}$$

By summing up the rates at which KE and PE of the various currents change within the control volume $BDGJ$, we obtain an expression for the net rate of change of mechanical energy within $BDGJ$, $\dot{E}^*_{BDGJ}$. Interestingly, $\dot{E}^*_{BDGJ}$ is always positive for any nonequal combination of (ρ^*_c, d^*_l) (see Fig. 24). Additionally, we can analyze the energy fluxes across the right and left boundaries

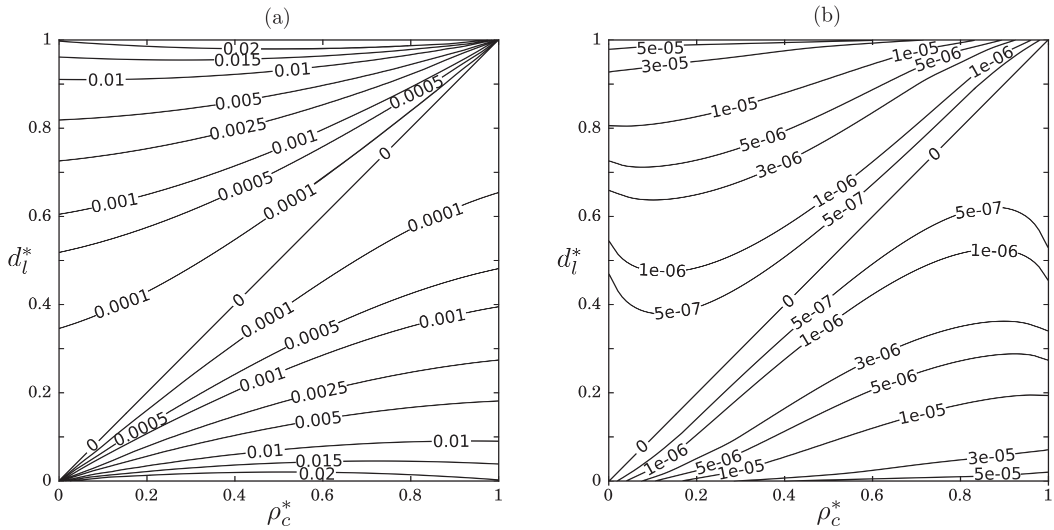

FIG. 25. Phase-space diagrams for the dissipated fraction of (a) the convective energy flux into $DEFG$, $-\dot{E}_{rs}^*$, ($|\Delta\dot{E}_b^*/\dot{E}_{rs}^*|$) and (b) the released potential energy within control volume $ADGK$ ($|\Delta\dot{E}_t^*/\dot{E}_{p,ADGK}^*|$).

into $BDGJ$ as

$$\dot{E}_{rs}^* = \tfrac{1}{2}(1-h_b^*)U_{ub}^{*3} - \tfrac{1}{2}h_b^*U_{lb}^{*3}, \tag{86}$$

$$\dot{E}_{ls}^* = \tfrac{1}{2}(1-h_u^*)U_{bc}^{*3} - \tfrac{1}{2}h_u^*U_u^{*3}. \tag{87}$$

Here $\dot{E}_{rs}^*$ and $\dot{E}_{ls}^*$ represent the energy fluxes into $BDGJ$ from the right and left boundaries, respectively. The energy budgets for the control volumes $BDD'B'$ and $B'D'GJ$ can be evaluated correspondingly and provide separate insight into the energetics of the control volumes encompassing the lower and upper gravity currents [see Figs. 24(b) and 24(c)].

We can assess the energetics associated with the leading bore by analyzing the rates of change of KE and PE in the control volume $DEFG$. In this way, we obtain

$$\dot{E}_{k,b} = \tfrac{1}{2}\rho_c U_b\big[U_{lb}^2 h_b + U_{ub}^2(H-h_b)\big], \tag{88}$$

$$\dot{E}_{p,b} = \tfrac{1}{2}(\rho_l-\rho_u)g\big(h_b^2-d_l^2\big)U_b. \tag{89}$$

Nondimensionalizing equations (88) and (89) results in

$$\dot{E}_{k,b}^* = \tfrac{1}{2}U_b^*\big[{U_{lb}^*}^2 h_b^* + U_{ub}^{*2}(1-h_b^*)\big], \tag{90}$$

$$\dot{E}_{p,b}^* = \tfrac{1}{2}\big(h_b^{*2}-d_l^{*2}\big)U_b^*. \tag{91}$$

Adding these two expressions yields the rate $\dot{E}_b^*$ at which the total mechanical energy within control volume $DEFG$ increases, as the propagating bore sets both fluid layers in motion and also raises the center of gravity of the dense fluid. By subtracting $\dot{E}_b^*$ from the entering energy flux, we obtain the portion of this energy influx that is dissipated by the bore $\Delta\dot{E}_b^*$ [see Fig. 25(a)]. We find that for the intrusions in the vicinity of the equilibrium condition, a small fraction of 0.01% of the entering energy flux is dissipated. Far away from equilibrium, on the other hand, this fraction can exceed 2%.

A corresponding evaluation of the energy within control volume $ABJK$ yields

$$\dot{E}_{k,lw} = \tfrac{1}{2}\rho_c U_l\big[U_u^2 h_u + U_{bc}^2(H - h_u)\big], \tag{92}$$

$$\dot{E}_{p,lw} = \tfrac{1}{2}(\rho_u - \rho_c)g[H^2 - (H - h_u)^2]U_l, \tag{93}$$

which in dimensionless form reads

$$\dot{E}^*_{k,lw} = \tfrac{1}{2}U_l^*\big[U_u^{*2} h_u^* + U_{bc}^{*2}(1 - h_u^*)\big], \tag{94}$$

$$\dot{E}^*_{p,lw} = -\tfrac{1}{2}\rho_c^*[1 - (1 - h_u^*)^2]U_l^*. \tag{95}$$

The rate $\dot{E}^*_{p,ADGK}$ at which PE is released in control volume $ADGK$ can be obtained by summing up Eqs. (83)–(85) and (95). The rate $\Delta\dot{E}_t^*$ at which mechanical energy inside $ADGK$ is dissipated is found by subtracting from $\dot{E}^*_{p,ADGK}$ the rate at which KE of the various currents grows, as well as the rate at which energy is being transferred to the leading bore across the boundary DG,

$$\Delta\dot{E}_t^* = \dot{E}^*_{p,ADGK} - \dot{E}^*_{k,c} - \dot{E}^*_{k,u} - \dot{E}^*_{k,l} + \dot{E}^*_{rs}. \tag{96}$$

Figure 25(b) displays the fraction of the released potential energy that is dissipated, $|\Delta\dot{E}_t^*/\dot{E}^*_{p,ADGK}|$. We find this fraction to be small for the entire range of ρ_c^* and d_l^*.

A further interesting question concerns the fraction of the potential energy released in $ADGK$ that is used to support the leading bore, i.e., the ratio $|\dot{E}_b^*/\dot{E}^*_{p,ADGK}|$. Figure 24 shows that for nearly symmetric conditions, the fraction of PE extracted by the leading bore is on the order of a few percent. However, for strongly nonsymmetric cases it can reach up to 20%. This confirms that the assumption by Cheong *et al.* [7], who neglected the effect of the bore on the overall energetics of the flow, is most accurate for nearly symmetric intrusions.

VII. INFLUENCE OF Re AND Pe

As described earlier, our DNSs employed finite values of the Reynolds and Péclet numbers. In light of the fact that earlier studies such as [23] had observed a certain dependence of the gravity

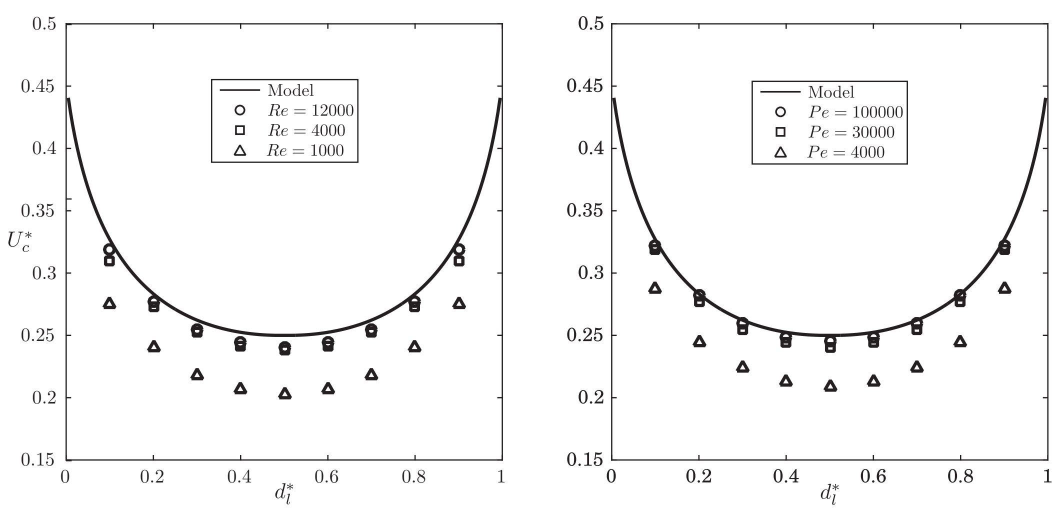

FIG. 26. Influence of the Reynolds (left) and Péclet (right) numbers on the intrusion velocity. On the left graph Pe = 30 000 and on the right one Re = 12 000. The DNS results are shown to approach the vorticity model predictions as Re and Pe increase.

current velocity on Re, it is hence of interest to investigate how the comparison between the DNS results and the inviscid vorticity model predictions is affected by changes in Re and Pe. Figure 26 provides information on this issue, for $\rho_c^* = 0.5$ and $0 < d_l^* < 1$. For the left graph, where we investigate the effect of the Reynolds number, Pe is held constant at 30 000 in all the simulations. For all parameter values, the intrusion velocity is shown to increase with Re, yielding closer agreement with the model predictions. For the right graph, where we focus on the influence of the Péclet number, Re is held fixed at 12 000. The numerical intrusion speed uniformly approaches the vorticity model prediction as Pe is increased. When Re and Pe are above 4000 and 30 000, respectively, the intrusion velocity no longer depends strongly on Re or Pe for intermediate values of d_l^*. However, for $d_l^* \approx 0$ or 1, the gravity currents developing along the upper or lower walls are quite thin, so the DNS results remain more sensitive to changes in Re or Pe.

VIII. CONCLUSION

We have employed the laws of mass and momentum conservation to develop a closed model for intrusive gravity currents propagating along the interface of a two-layer stratified ambient. Based on the vorticity form of the momentum-conservation principle, the model does not require any empirical closure assumptions. Using this model, we conduct a detailed parametric study in terms of the dimensionless intrusion density and the lower layer height of the ambient, which reproduces the correct behavior for all known limits and confirms many previous experimental observations. Specifically, the present model demonstrates that the conservation of mass and momentum dictates the formation of equilibrium flows when the intrusion density equals the depth-weighted mean density of the two ambient layers, consistent with the observations by Sutherland *et al.* [6]. These equilibrium intrusions are shown to correspond to classical energy-conserving gravity currents with a thickness of half the channel height.

The parametric study confirms that for a fixed intrusion density, the equilibrium configuration corresponds to the minimum propagation velocity, in agreement with the experimental observations of Cheong *et al.* [7]. The model furthermore demonstrates that the limits of $(\rho_c^* = 0, d_l^* = 1)$ and $(\rho_c^* = 1, d_l^* = 0)$ are not smooth, in the sense that the height of the leading bore does not uniformly go to zero, so the solution does not smoothly approach the case of a classical lock-exchange gravity current. The bore height smoothly approaches zero and its velocity reduces to that of a linear wave as the intrusion nears equilibrium conditions. In addition, the bore height is shown to vary linearly with $|\rho_c^* - d_l^*|$, consistent with earlier observations in Refs. [7,8]. An *a posteriori* energy analysis demonstrates that under nonequilibrium conditions the intrusion *gains* energy.

The predictions by the parametric study are furthermore compared to two-dimensional DNS results and very good agreement is found with regard to all flow properties, including the propagation velocities of the intrusion and the gravity currents, their thickness, and the height and velocity of the leading bore.

ACKNOWLEDGMENT

We gratefully acknowledge support through NSF Grant No. CBET-1335148.

[1] J. E. Simpson, D. A. Mansfield, and J. R. Milford, Inland peneration of seabreeze fronts, Q. J. R. Meteorol. Soc. **103**, 47 (1977).

[2] E. J. Hopfinger, Snow avalanche motion and related phenomena, Annu. Rev. Fluid Mech. **15**, 47 (1983).

[3] J. E. Simpson, *Gravity Currents*, 2nd ed. (Cambridge University Press, Cambridge, 1997).

[4] B. R. Sutherland, *An Introduction to Gravity Currents and Intrusions* (CRC, Boca Raton, 2010).

[5] J. Y. Holyer and H. E. Huppert, Gravity currents entering a two-layer fluid, J. Fluid Mech. **100**, 739 (1980).

[6] B. R. Sutherland, P. J. Kyba, and M. R. Flynn, The front speed of intrusive gravity currents, J. Fluid Mech. **514**, 327 (2004).
[7] H.-B. Cheong, J. J. P. Kuenen, and P. F. Linden, The front speed of intrusive gravity currents, J. Fluid Mech. **552**, 1 (2006).
[8] M. R. Flynn and P. F. Linden, Intrusive gravity currents, J. Fluid Mech. **568**, 193 (2006).
[9] R. E. Britter and J. E. Simpson, A note on the structure of the head of an intrusive gravity currents, J. Fluid Mech. **112**, 459 (1981).
[10] T. B. Benjamin, Gravity currents and related phenomena, J. Fluid Mech. **31**, 209 (1968).
[11] F. de Rooij, P. F. Linden, and S. B. Dalziel, Saline and particle-driven interfacial intrusions, J. Fluid Mech. **389**, 303 (1999).
[12] R. J. Lowe, P. F. Linden, and J. W. Rottman, A laboratory study of the velocity structure in an intrusive gravity current, J. Fluid Mech. **456**, 33 (2002).
[13] B. R. Sutherland, Interfacial gravity currents. I. mixing and entrainment, Phys. Fluids **14**, 2244 (2002).
[14] A. Mehta, B. R. Sutherland, and B. J. Kybia, Interfacial gravity currents. II. Wave excitation, Phys. Fluids **14**, 3558 (2002).
[15] S. K. Ooi, G. Constantinescu, and L. Weber, 2D large-eddy simulation of lock-exchange gravity current flows at high Grashof numbers, J. Hydraul. Eng. **133**, 1037 (2007).
[16] Z. Borden and E. Meiburg, Circulation-based models for Boussinesq gravity currents, Phys. Fluids **25**, 101301 (2013).
[17] Z. Borden and E. Meiburg, Circulation-based models for Boussinesq internal bores, J. Fluid Mech. **726**, R1 (2013).
[18] N. Konopliv, S. G. Llewellyn Smith, and E. Meiburg, Modeling gravity currents without an energy closure, J. Fluid Mech. **789**, 806 (2016).
[19] M. M. Nasr-Azadani and E. Meiburg, Gravity currents propagating into shear, J. Fluid Mech. **778**, 552 (2015).
[20] M. M. Nasr-Azadani and E. Meiburg, Gravity currents propagating into ambients with arbitrary shear and density stratification: Vorticity-based modeling, Q. J. R. Meteorol. Soc. **142**, 1359 (2016).
[21] M. M. Nasr-Azadani and E. Meiburg, Turbins: An immersed boundary, Navier-Stokes code for simulation of gravity and turbidity currents interacting with complex topographies, J. Comput. Fluids **45**, 14 (2011).
[22] M. M. Nasr-Azadani, B. Hall, and E. Meiburg, Polydisperse turbidity currents propagating over complex topography: Comparison of experimental and depth-resolved simulation results, Comput. Geosci. **53**, 141 (2013).
[23] C. Härtel, E. Meiburg, and F. Necker, Analysis and direct numerical simulation of the flow at a gravity-current head. Part 1. Flow topology and front speed for slip and no-slip boundaries, J. Fluid Mech. **418**, 189 (2000).